UNIVERSITY OF TWENTE.

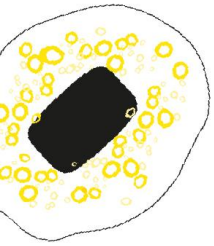

University of Twente

Assessment of the MR compatibility of a subcutaneous migraine implant

MSc Thesis – Biomedical Engineering

Geurink, B.M.
10-7-2024

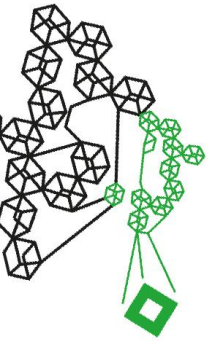

Graduation Committee

Prof. dr. S. Manohar	-	Chair
Dr.ir. W.M. Brink	-	Supervisor
Dr.ir. W. Rensen	-	Supervisor
Prof. dr. ir. N.J.J. Verdonschot	-	External member

Magnetic Detection & Imaging (MD&I)
Multi-Modality Medical Imaging (M3I)

Abstract

Migraine is a neurological disorder that affects up to 15 percent of the adult population and is associated with a significant socio-economic burden and reduction in quality of life. Conventional treatment methods are often ineffective and cause severe side effects.

This research investigates the MR compatibility of a novel subcutaneous neurostimulation device designed to relieve the symptomology of (chronic) migraine. Its unique characteristics with respect to other neurostimulators raises interest and need for a dedicated evaluation of its safety within an MRI environment (mainly 1.5T). The ISO/TS 10974:2018 on the MR compatibility of Active Implantable Medical Devices (AIMD) provided a framework for the experimental setup including the evaluation of translational force, torque and demagnetisation induced by the static magnetic field (B_0), RF- and gradient induced heating, functionality of the AIMD after exposure to the electromagnetic fields of an MRI and an assessment of the induced image artifacts.

Results have shown that the AIMD experienced reasonable translational forces (max. 1 N) and substantial torque (max. 0.068 Nm). No demagnetisation was found for 1.5T systems. 3.0T and 7.0T systems resulted in significant orientational dependent demagnetisation (>100%). The simulated RF induced heating amounted to max. ±2.3 W/kg with hotspots localized near the eighth electrode of the lead. Experimentally, a temperature increase of max. 1.28 °C was found. Gradient induced heating was not observed. None of the experiments caused dysfunctionality of the AIMD.

These findings seem to offer a good perspective for MR compatibility labelling in 1.5T systems. However, the torque can potentially be problematic and lead to dislocation or rotation of the internal magnet or the AIMD. The max. RF-induced heating is also not compliant with the safety limit. However, this is a conservative analysis which means less significant heating may occur in practice. In addition, a CEM43 analysis showed that the risk of tissue damage due to heating is minimal.

Abstract (Dutch)

Migraine is een neurologische aandoening die tot 15 procent van de volwassen bevolking treft en gepaard gaat met een aanzienlijke sociaaleconomische druk en een verminderde kwaliteit van leven. Conventionele behandelmethoden zijn vaak ineffectief en veroorzaken ernstige bijwerkingen.

In dit onderzoek wordt de MR-compatibiliteit van een nieuw subcutaan neurostimulatie implantaat onderzocht. Dit implantaat is ontworpen om de symptomen van (chronische) migraine te verlichten. De unieke eigenschappen van dit implantaat ten opzichte van andere neurostimulatoren wekken de interesse in en de behoefte aan een toegewijde evaluatie van de veiligheid in een MRI scanner (voornamelijk 1.5T). De ISO/TS 10974:2018 over de MR-compatibiliteit van Actieve Implanteerbare Medische Hulpmiddelen (AIMD) vormde het kader voor de experimentele opzet, waaronder de evaluatie van aantrekkingskracht, torsie en demagnetisatie geïnduceerd door het statische magneetveld (B_0), RF- en gradiënt geïnduceerde opwarming, functionaliteit van de AIMD na blootstelling aan de elektromagnetische velden van een MRI en een beoordeling van de geïnduceerde beeldartefacten.

De resultaten toonden aan dat de AIMD een matige aantrekkingskracht ondervond (max. 1 N), maar vooral een aanzienlijke torsie (max. 0.068 Nm). Er werd geen demagnetisatie gevonden voor 1.5T systemen. 3.0T en 7.0T systemen resulteerden in significante oriëntatieafhankelijke demagnetisatie (>100%). De gesimuleerde RF geïnduceerde opwarming bedroeg max. ±2.3 W/kg met hotspots rondom de achtste elektrode van de lead. Experimenteel is een maximale temperatuurstijging van 1.28 °C waargenomen. Gradiënt geïnduceerde opwarming is niet geconstateerd. Tevens heeft geen van de testen geleidt tot disfunctionaliteit van de AIMD.

Deze resultaten lijken een goed perspectief te bieden voor MR-compatibiliteit in 1.5T-systemen. Echter, de torsie kan mogelijk problematisch zijn en kan leiden tot dislocatie of rotatie van de interne magneet of de gehele AIMD. Ook de max. RF geïnduceerde opwarming voldoet niet aan de veiligheidslimiet. Echter, dit is een conservatieve analyse waardoor er in de werkelijkheid mogelijk minder significante opwarming zal plaatsvinden. Daarbij laat een CEM43-analyse zien dat de kans op weefselschade ten gevolge van de opwarming minimaal is.

Table of Contents

Acknowledgement

I want to express great gratitude to Prof. Dr. Thijs van Osch for facilitating the experiments on the 3.0T and 7.0T systems, Jaap Greve for his support during several experiments and Dr. Ir. Wyger Brink and Dr. Ir. Wouter Rensen for providing supervision, guidance and valuable moments of discussion throughout the project.

1. Introduction

Migraine is a common neurological disorder that affects roughly one billion people worldwide. The Global Burden Disease study (2019) has classified migraine as the second most common cause of disability [1]. It is estimated that in Europe, about 15 percent of the adult population suffers from episodic migraine with the prevalence among the female population (22 percent) being greater in comparison to the male population (8 percent) [2][3]. It is estimated that of this 15 percent, 2 to 8 percent can be classified as chronic migraine [3]. Economic research has found an annual burden of EUR 2.4 to 4.2 billion for the Dutch society due to reduced productivity as a result of migraine [4]. These statistics include both episodic migraine and chronic migraine. Episodic migraine considers the patient population that suffers from migraine for less than 15 days a month. The International Classification of Headache Disorders 3rd Edition has characterised chronic migraine as the condition of having a minimum of 15 headache days a month of which at least eight days must meet the symptom criteria for migraine. If this pattern persists for at least three months, it is referred to as chronic migraine. Chronic migraine is associated with significant debilitation, loss of productivity and a severe socio-economic burden worldwide. Estimates indicate that, in Europe, the socio-economic burden and the treatment of patients with chronic migraine amounts to roughly EUR 95 billion annually [3].

Treatment of chronic migraine focusses on reduction of the frequency and severity of migraine attacks. Physicians often base their treatment plan on both non-drug interventions such as lifestyle counselling and patient tailored drug therapy [3]. However, the effectiveness of these treatment methods is often lacking due to, inter alia, adverse effects of medication. The willingness of patients to persist with preventive migraine medication treatment is found to be limited. Only 25 percent of patients decide to continue drug therapy after 6 months with a mere 14 percent persistence after 12 months [5]. Another study found that the willingness to take preventative medication was less than 60 percent, even if the drug therapy would result in a 50 percent decrease in headache frequency [5]. Because of this, there is an increasing interest into medication-free treatment approaches such as neuromodulation. Neuromodulation, also referred to as neurostimulation, is a treatment approach that makes use of electrical or magnetic stimulation of nerves [3]. Stimulation of specific nerves is aimed at suppressing migraine symptoms and the potential of both non-invasive and invasive neuromodulation devices is being investigated [3]. Occipital nerve stimulation (ONS) is a promising neuromodulation technique aimed at relieving migraine symptomatology. This involves subcutaneous implantation of a device consisting of a lead with electrodes that deliver the electrical stimuli to the targeted nerve and an implantable pulse generator (IPG) that controls these electrical stimuli [6].

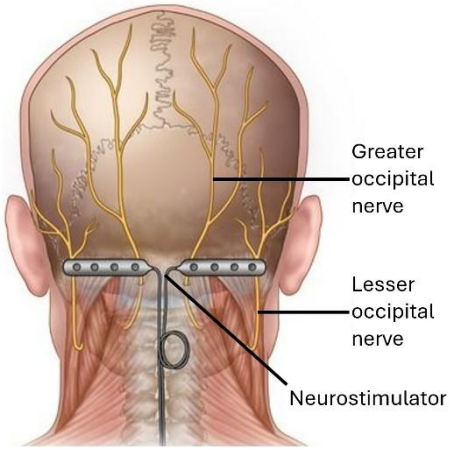

Figure 1 Visual example of occipital nerve stimulation (ONS) [7]

Although the placement of such an implantable device may greatly improve the patient's quality of life, it also introduces a number of risks. One potential hazard when having an implanted device is, for instance, undergoing an MRI scan [8]. Magnetic Resonance Imaging (MRI) is a radiation-free imaging modality that has been widely adopted in the field of medical imaging and diagnostics. The technique offers superior soft-tissue contrast and high resolution imaging, which has made it the golden standard for diagnosis of numerous pathologies [8]. Therefore, it is

not desirable that implantation of a device renders the patient unable to undergo an MRI scan because of safety concerns. For this reason, extensive research and development is conducted into establishing safety limits and operating procedures to ensure that both patients with passive- and active implants can safely undergo MRI scans again [8][9][10]. This research concentrates on the analysis of the safety hazards that arise when a patient with an active implantable medical device (AIMD) needs to undergo an MRI scan. An AIMD is defined as an implantable device whose function is reliant on a source of (electrical) energy that is not generated by the human body itself or gravity [10]. For the assessment of the safety of AIMDs in an MRI environment, the ISO/TS 10974:2018 standard was established. This international technical specification entitled *"Assessment of the safety of magnetic resonance imaging for patients with an active implantable medical device"* outlines the hazards that arise when a patient with an AIMD undergoes an MRI scan [11]. The standard guides AIMD manufacturers in the safety assessment of their implantable device by describing a set of test methods that measure the extent to which potential hazards in the MRI environment are manifested. For the acquisition of a magnetic resonance image, three electromagnetic (EM) fields are important: (1) the static magnetic field (B_0), (2) the radiofrequency (RF) field (B_1) and (3) the gradient field (G). Each of these EM fields may cause a number of potential interactions with the implanted AIMD that influence patient safety. These interactions are outlined in Table 1 [11].

Table 1 Potential safety hazards, inducing mechanism and associated ISO/TS 10974:2018 clause [11]

Hazard	Mechanism	ISO Clause
Heating	RF induced heating	8
	Gradient induced heating	9
Vibration	Gradient induced vibrations	10
Force	B_0 induced force	11
Torque	B_0 induced torque	12
Unintended Stimulation	Gradient induced lead voltage (extrinsic electric potential)	13
	RF induced rectified lead voltage	
Malfunction	B_0 induced malfunction	14
	RF induced malfunction	15
	Gradient induced malfunction	16
	Combined Fields test	17

This research considers an AIMD that is under development with the intent to relieve the symptoms of (chronic) migraine. This neurostimulation device is designed to stimulate the nerves that are associated with the condition using minor electrical pulses. The device is positioned behind the scalp, in front of the skull, on both sides of the head of the patient and is targeted to stimulate the occipital- (ONS) and supraorbital nerves (SONS). Even though a considerable amount of research has been conducted on other neurostimulation devices such as cochlear implants (CI) and deep brain stimulators (DBS), the AIMD considered in this research has several exceptional characteristics that renders it incomparable to CI and DBS devices. This includes the fact that the AIMD is implanted epicranially without any transcranial components, the ultra-thin design and the full silicone casing. Also, according to regulations, each device has to be examined individually in order to make justified statements about its MR compatibility.

The goal of this research is to evaluate the MR compatibility of the first version of the novel neurostimulator. This reveals the potential hazards patients with the current version of the AIMD may be exposed to once they come into contact with MRI and allows for identification of any potential safety concerns that should be taken into consideration during the design process of future versions of the AIMD. The goal is subdivided into the assessment of the interactions with

(1) the static magnetic field (B_0), (2) the radiofrequency field (B_1) and (3) the gradient field (G) and consists of the following elements:

1. *What is the magnitude of the translational forces induced by B_0?*
2. *What is the magnitude of the torque induced by B_0?*
3. *To what extent does B_0 induce demagnetisation of the internal magnet of the AIMD?*
4. *Do gradient induced vibrations cause dysfunctionality of the AIMD?*
5. *What is the magnitude of gradient induced heating of the AIMD?*
6. *What is the magnitude of RF induced heating of the AIMD?*
7. *Does a Combined Fields Test cause dysfunctionality of the AIMD?*
8. *To what extent do image artifacts reduce the diagnostic capability in neuroimaging?*

In general, this scope is in line with the requirements of ISO/TS 10974:2018. However, some elements of this technical standard are excluded from the scope of this exploratory research. That is, clause 13 (Table 1) that considers unintended stimulation which is not included due to the unique characteristics of the tested AIMD for which the clause, currently, does not define specific experiments that conclusively determine the degree of unintended stimulation. Also, determining the degree of unintended stimulation does not require an MRI scanner but uses tissue interface injection networks and RF / gradient field generators which are not at our disposal. This also applies to clauses 15 and 16 that assess device malfunction due to RF and gradient fields since these clauses require exposing the AIMD to worst-case RF and gradient scenarios which cannot be reproduced on a clinical MRI scanner. Clause 8 requires RF-induced heating to be determined using a model that is validated in vitro. In principle, the same procedure is followed in this study but a simplified heating model will be established given the exploratory nature of this study and the complexity of a model that complies with the set standard. As a first step, the potential risk of RF-induced heating will be estimated by incorporating conservative conditions into the model. More elaborate computer simulations using heterogeneous body models and positioning of the AIMD may extend this assessment but this is beyond the scope of the current work. In contrast, demagnetisation of the AIMD magnet and induced image artifacts are not included in the ISO/TS 10974:2018 but were included in this study. This is because maintaining a functional internal magnet is crucial for the functionality of the AIMD while assessment of the size of the image artifacts will provide an important impression of the extent to which the AIMD reduces the diagnostic capability in neuroimaging.

Although the ISO/TS 10974:2018 provides guidance on the assessment of the MR compatibility of an AIMD, it is unknown to what extent the outlined interactions occur with the AIMD in this research given its unique characteristics. Also, the standard defines general test methods and the exact methodology of the assessment should be adapted to the characteristics of the AIMD in order to optimise the assessment. This paper will first present an outlook on the hypothesised interactions with the three electromagnetic fields and explain the safety limits that should be considered in Chapter 2. Then, Chapter 3 will describe the methodology of the experiments in the order of the three electromagnetic field, followed by the results in Chapter 4.

2. Theory

MR imaging is based on the interplay of three electromagnetic (EM) fields: (1) the static magnetic field (B_0), (2) the radio frequency field (B_1) and (3) the gradient field (G). These three fields all contribute in a distinct way to create an image of the inside of the body based on their interaction with proton spins [12]. This chapter explains the physical principles of these three EM fields, their role in MR-image acquisition and the physics behind the potential safety hazards induced by the EM fields.

2.1 Static Magnetic Field (B_0)

The static magnetic field (B_0) is the most distinctive feature of MRI systems. Super-conducting magnets with a horizontal bore are most often used in clinical MRI systems to create magnetic fields of 1.5 to 3 Tesla (T) [12]. Obtaining a strong and homogeneous B_0 field is the first step towards the acquisition of an MR image. The signal that forms the MR image originates from the 'spin' of the hydrogen atoms in the body. The nucleus of a hydrogen atom consists of a proton having a quantum mechanical property, referred to as 'spin', which causes it to induce its own very small magnetic dipole moment [12]. The protons would normally have a random spin but in the presence of a strong external magnetic field, the spins align. This alignment constitutes a cumulative vector of spins having a far stronger magnetisation than the individual spins, the net magnetisation vector (M_0), which is measurable [12].

Interaction Mechanisms

To understand the safety hazards and interactions in the vicinity of the magnetic field of an MRI scanner, two properties of the magnetic field are particularly important: (1) the magnetic field strength (B) in units of Tesla and (2) the spatial gradient of the magnetic field ($\boldsymbol{\nabla} B$) in Tesla per meter [13]. These properties are unique for each MRI system. Figure 2 shows spatial maps of the B_0 field (T) and the spatial gradient ($\mathrm{T/m}$) of the B_0 field of a Siemens Prisma 3.0T scanner [14]. These properties determine the translational and rotational forces that are exerted on objects near the magnet.

The interaction with the static field also depends on the material properties of the object that is exposed. Ferromagnetic materials will interact significantly with the B_0 field while dia- and paramagnetic materials will experience little to no interaction [13]. The forces that act on a ferromagnetic object in the vicinity of an MRI scanner depend on the magnetic dipole moment (m) of the object. The magnetic dipole moment can be calculated using Eq. 2.1 [13] with: B_r the remanence of the ferromagnetic material, V its volume and μ_0 the permeability of vacuum.

$$\boldsymbol{m} = \frac{1}{\mu_0} B_r V \tag{2.1}$$

Translational Force

The translational force is dependent on the spatial gradient of B_0 and can be determined through the dot product of the magnetic dipole moment and the spatial gradient of B_0, Eq. 2.2 [13]. For a patient entering the scanner, the translational force is maximum around the entrance of bore given that at this location, ∇B is the very large. ∇B is the greatest at the periphery of the bore itself, see Figure 2B. However, this spatial gradient is less relevant because a patient is unlikely to move across this gradient.

$$F_{trans} = \boldsymbol{m} \cdot \boldsymbol{\nabla} B_0 \tag{2.2}$$

Torque

The rotational force (torque) depends on the strength of the magnetic field and will thus be maximal around the isocentre of the scanner, see Figure 2A. The torque on a ferromagnetic material can be calculated through the vector product of the magnetic dipole moment and the field strength (B), Eq. 2.3 [13].

$$\tau_m = \boldsymbol{m} \times \boldsymbol{B} \tag{2.3}$$

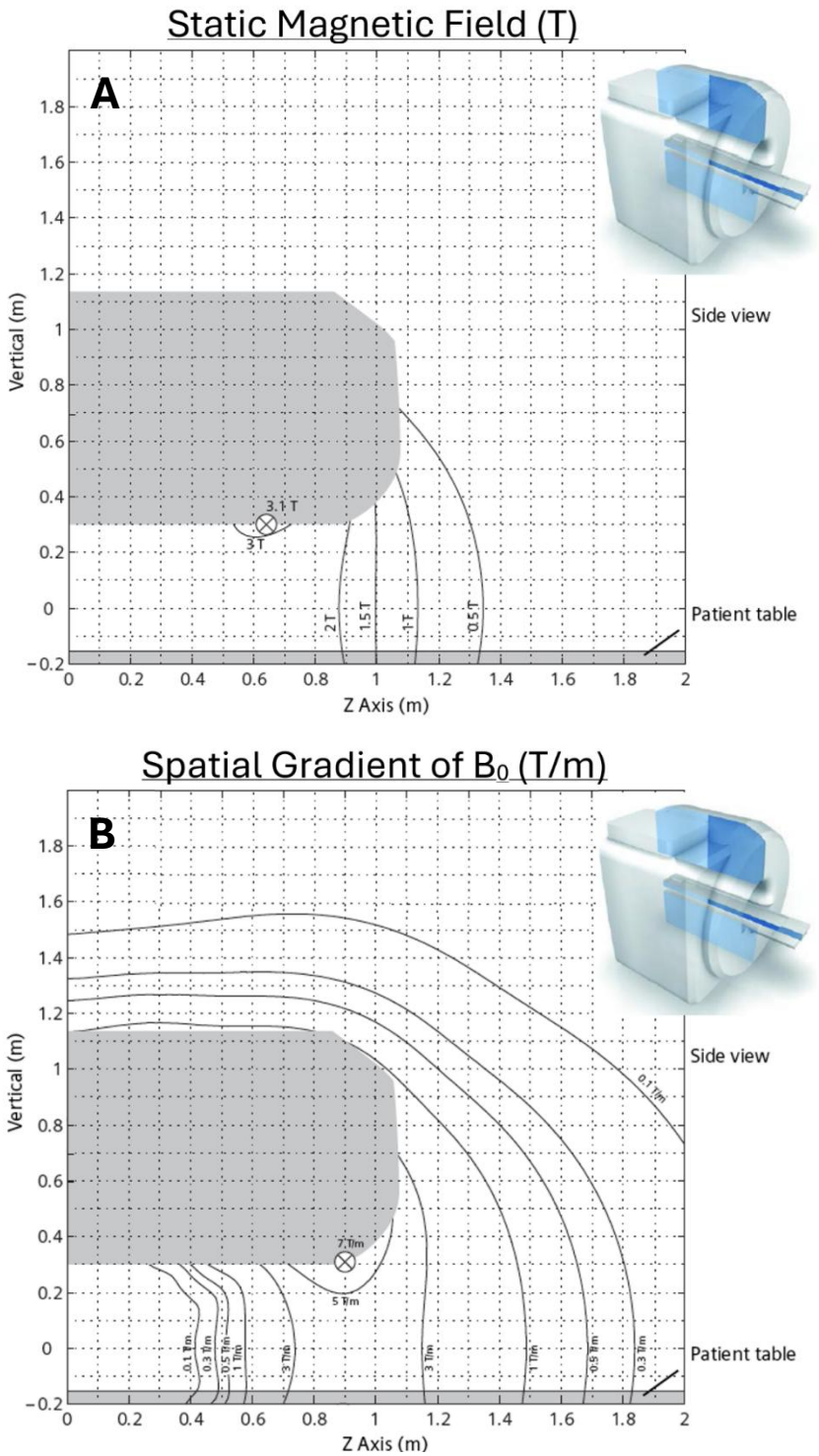

Figure 2 A) Visualisation of the strength of the static magnetic field around a Siemens Prisma 3.0T scanner. B) Visualisation of the spatial gradient of the static magnetic field around a Siemens Prisma 3.0T scanner [14]

Given Eq. 2.1 to 2.3 and the properties of the object, the theoretical translational and rotational forces can be determined. The forces acting on the AIMD that is analysed in this research originate mainly from the internal magnet (NdFeB, Grade: N50EH). The magnet has a remanence of $1.407\ \mathrm{T}$ and volume of roughly $9.24 \cdot 10^{-8}\ \mathrm{m}^3$. From this, the magnetic dipole moment can be determined ($m = 0.1035\ \mathrm{A} \cdot \mathrm{m}^2$) which can then be used to determine the translational and rotational forces for the Siemens Magnetom Aera 1.5T with ∇B_0 = 3 $\mathrm{T/m}$ and B = 1.5 T [12]:

$$F_{m\_trans} = \boldsymbol{m} \cdot \boldsymbol{\nabla} B_0 = 0.1035 \cdot 3 = 0.3105\ \mathrm{N}$$

$$F_{m\_rot} = \boldsymbol{\tau_m} = \boldsymbol{m} \times \boldsymbol{B} = 0.1035 \cdot 1.5 = 0.16\ \mathrm{Nm}$$

ISO/TS 10974:2018 acceptance criteria are met if the magnetically induced forces are less than the gravitational forces acting on the device. However, given the ultra-light and small design of the AIMD, it is likely that the gravity criterion is not met. Simply because gravitational forces that act on the device are very minimal and easily exceeded. Thus, the risk of the magnetically induced forces will be compared to the forces that act on cochlear implants that have already obtained MR compatibility labelling. Eerkens et. al. [26] analysed the translational and rotational forces of several generations of CIs with MRI compatibility labelling. Translational forces of about 0.4 N at bore entrance to a maximum of 1.8 N have been found for CIs [26]. Here, it is important to mention that Eerkens et. al. also considers the maximum achievable translational force. Due to active shielding of MRI scanners, the spatial gradient (∇B) at the edge of the scanner bore is often higher than at the entrance of the bore. Documentation shows that the Siemens Magnetom Aera 1.5T has a maximum ∇B of 11 $\mathrm{T/m}$, while the Philips Achieva TX 3.0T has a ∇B of 7 $\mathrm{T/m}$ [12][15]. The exact gradient of the 7.0T system is unknown but likely lower since this scanner is not actively shielded. This means that theoretically, the maximum translational forces are estimated to be 1.14 N for the 1.5T system and 0.72 N for the 3.0T system.

Eerkens et. al. converts the torque to a force acting on the edge of the AIMD using the diameter of the stimulator unit of the AIMD (r). A maximal force acting on the stimulator of roughly 5 N was found for older models of CIs. Newer models of CIs incorporate a diametric or fully rotating magnet that reduces the torque resulting in a force as low as 3 N [26]. The maximal translational force of 1.8 N and rotational force of 5 N acting on the stimulator will be considered the safety limit in this research considering axial magnets. Last, the measurements will be compared to the torque found for a Cochlear Implant with a rotatable magnet, 0.043 Nm [27]. This figure is not necessarily a distinct safety limit but gives an idea of the minimal torque with which current devices have obtained MRI compatibility labelling.

Demagnetisation

Another factor that does not directly pose a threat to patient safety but can greatly affect the functionality of the AIMD is demagnetisation of the internal magnet after exposure to B_0. The risk of demagnetisation of the internal magnet is that the transcutaneous coupling may slip or become dysfunctional. However, no specific degree of demagnetisation after which the coupling is considered impaired has been established. It is hypothesised that demagnetisation of a few percent has no significant effect on the quality of transcutaneous coupling. Demagnetisation of the internal magnet is attributed to the fact that the individual magnetic domains in the magnet start to align with B_0 [13]. The extent of this effect depends on the strength of the external magnetic field and magnetic anisotropy. The susceptibility of the AIMD magnet to various external magnetic field strengths is shown in Figure 3 [15]. This figure shows the BH-curve of the NdFeB N50EH magnet. The graph shows that for an external field strength of 1.5T (red line), there will be minimal demagnetisation of up to a few percent. The magnet will be reasonably robust against demagnetisation up to a field strength of 3.0T (purple line), plus minus 12 percent. Given that the purple line of 3.0T is already in the deflecting section of the graph, field strengths greater than 3.0T are likely to lead to complete demagnetisation of the AIMD magnet.

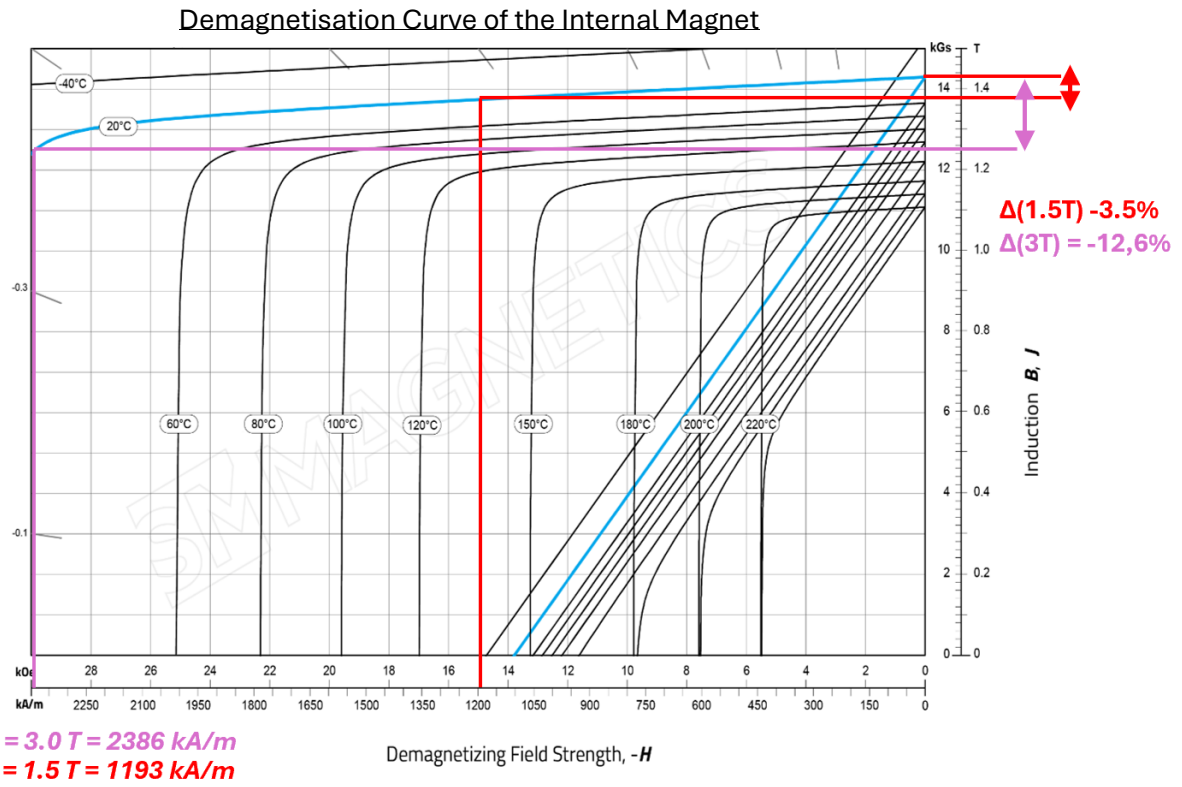

Figure 3 Demagnetisation (BH) Curve of the AIMD magnet [15]

In addition to the external field strength, magnetic shape anisotropy which is manifested through the demagnetizing field is also involved in the process of (de)magnetisation. The demagnetizing field of an object depends on its shape and orientation with respect to B_0 [13]. This dependence is explained by the interaction between the individual dipoles inside the magnet [16]. Although literature mainly describes the influence of the demagnetizing field for magnetisation of ferromagnetic materials, we hypothesize that this theory can be applied similarly to the opposite principle, demagnetisation. In ferromagnetic materials, a large percentage of the spins in the magnetic domains aligns with the external field B_0 causing the individual dipoles of the magnetic domains to overlap, partially cancelling each other. This results in a demagnetizing field and makes it energetically more favourable for an object to be magnetised along its main axis (easy axis) than orthogonally to its main axis (hard axis) [16][17][18].

The demagnetisation factor (N) correlates to the size of the demagnetizing field of the magnet. The size of the demagnetizing field indicates the amount of energy that is required to magnetise, or demagnetise, an object [16]. Demagnetisation factors are not easily determined and often require extensive numerical analysis. However, the approximation of the demagnetisation factor of a few symmetric objects is more convenient. Wysin [19] numerically determined the demagnetisation factor of a cylinder, which is the shape of the magnet embedded in the AIMD central to this research. This is shown in Eq. 2.4 [19] and the factors are calculated for the dimensions of the AIMD magnet ($R = 3.5, L = 2.4$).

$$N_z = \frac{1}{L}\left(L + R - \sqrt{L^2 + R^2}\right) = 0.69 \qquad N_x = N_y = \frac{1-N_z}{2} = 0.155 \tag{2.4}$$

The factor N has an important role when determining the degree of susceptibility of a ferromagnetic material to magnetisation. If the total internal magnetic field, i.e. the sum of the external magnetic field minus the demagnetizing field, is greater than the intrinsic coercivity (H_{ci}) of the internal magnet, magnetisation will occur. This is illustrated in Eq. 2.5. Herein, the demagnetizing field is given as the demagnetisation factor (N) times the magnetisation (M_r) with $M_r = \frac{B_r}{\mu_0}$ [16][19][20].

$$H_{internal} = H_{external} - H_{demagnetisatoin} = H_{external} - NM_r \tag{2.5}$$

This relationship illustrates that a larger N results in a smaller internal magnetic field strength, increasing the likelihood of not exceeding the coercivity of the magnet, and thus decreasing the likelihood of magnetisation. Conversely, a smaller N will cause the magnet to be more susceptible to magnetisation. Considering the result of Eq. 2.4 in the context of Eq. 2.5 for the AIMD magnet, the larger N_z implies that the magnet will magnetise less if it is aligned with the *z*-axis of the scanner. Conversely, there may be more substantial magnetisation if the magnet is oriented orthogonal to the *z*-axis (along the *x*-axis) because N_x is smaller. It is important to mention that the strength of the external magnetic field plays a major role. If this strength is much lower than the coercivity of the magnet, then there is no need to assess orientational dependence. However, if the external magnetic field is stronger than the coercivity, then the demagnetizing field can offer additional resistance to magnetisation

It is unknown whether this relation also applies to demagnetisation but the demagnetizing field may be an explanation for the orientational dependence of the (de)magnetisation of ferromagnetic materials as seen in literature [21][22] and warrants dedicated experimental assessment for the magnet used in the AIMD of this research.

2.2 Radiofrequency Field (B_1)

The static magnetic field establishes a foundation for an MR-image through the alignment of spins. However, more is required to create an actual signal. Although, theoretically the net magnetisation M_0 should yield a measurable signal, in reality it appears that it is practically impossible to measure M_0 whilst in equilibrium because it is in alignment with the much stronger B_0 field [12]. To solve this, a second electromagnetic field, the radio frequency (RF) field (B_1), is used. An RF-pulse is transmitted to flip M_0 towards the *x-y* (transverse) plane. The precession of the M_0-vector around the *z*-axis in the *x-y* plane causes an oscillating magnetic field that induces a voltage in a receive coil [12]. After excitation of the protons into the transverse plane, relaxation mechanisms take place that return M_0 to the equilibrium position. The exact course of the relaxation curve after excitation of the protons depends on the molecular environment of the protons and is the physical principle underlying the differentiation of tissues in MRI [12].

Specific Absorption Rate

The main safety consideration associated with the B_1 field is RF induced heating of tissues. The electric field that is associated with the magnetic field generated by the RF coils induces an electric current in the tissues. Ohmic resistance to these currents results in energy deposition in the form of heat [13]. In MRI, the rate of tissue heating is defined through the Specific Absorption Rate (SAR) which is defined as the power dissipated per unit volume divided by the mass density of the tissue, Eq. 2.6 [13][23].

$$\mathrm{SAR} = \frac{\sigma E_p^2}{2\rho} \tag{2.6}$$

The Specific Absorption Rate can be defined over the whole body, head, partial body or locally. The whole body- and head SAR approximations use the total mass or the mass of the patient's head, respectively. Partial body SAR accounts for the mass of the patient within the RF transmit coil. Local SAR is defined over any 10 grams of tissue. Considering that heating around the AIMD will be very localised and the heat is unlikely to dissipate further into the head, the local SAR limit is considered. The total rise in temperature in the medium (ΔT) can be approximated through multiplication of the SAR and the exposure time in seconds, divided by the heat capacity (C) of tissue, roughly 4200 J/kg/°C, see Eq. 2.7. [13]. The ISO/TS 10974:2018 (section 8.1) considers the SAR limits given in IEC 60601-2-33 in which the SAR is determined over an averaging time of six minutes (section 201.12.4.103.2, table 205.105 [24]). This implies a maximal temperature increase (local SAR) of roughly 0.85 degrees Celsius. SAR limits and the corresponding increase in temperature for all definitions is shown in Table 2.

$$\Delta T = \frac{\mathrm{SAR} \cdot t}{C} \tag{2.7}$$

Table 2 SAR limits as described in IEC 60601-2-33 and the corresponding temperature increase [24]

	Whole Body	***Head***	***Partial Body****	***Local***
SAR Limit (W//kg)	2	3.2	2 – 10	10
ΔT Limit (°C)	0.17	0.27	0.17 – 0.85	0.85

**Partial Body SAR scales with: exposed patient mass / total patient mass*

Although the ISO/TS 10974:2018 references the SAR limit established in the IEC 60601-2-33, this SAR limit is an indirect measure of the thermal risk involved with an MRI scan because this limit itself does not indicate anything about the potential biological damage caused by the heating. Therefore, the CEM43 which accounts for the biological effects of the RF induced heating is also often considered. This method examines the actual thermal dose received by a specific tissue type and relates it to potential harmful effects such as necrosis [25]. The CEM43 is defined in Eq. 2.8 for time interval (t), temperature (T), a temperature dependent scaling factor (R) and the number of samples (n_s) [25].

$$\mathrm{CEM43} = \sum_{i=1}^{n_s} t \cdot R^{43-T_i} \tag{2.8}$$

The CEM43 dose threshold is tissue dependent and amounts to 21 for AIMDs placed in skin tissue [25]. This implies that to meet the CEM43 requirement, the measured RF-induced heating has to translate into a CEM43 smaller than 21.

RF coupling: the 'antenna' effect

In addition to the global heating that occurs in tissue, additional local heating can occur around implants. This can have several sources but for the AIMD in this research, the antenna effect is particularly important [23]. This effect describes the resonant behaviour of RF currents induced in the lead of the AIMD when exposed to an electric field component parallel to the trajectory of the lead. These currents do not lead to heating of the lead itself, given the high conductivity of the material most leads are made of. Rather, heating is caused near the electrodes where the current flows into the resistive tissue [13]. The antenna effect is most prominent when the incident electric field is parallel to the lead, i.e. lead along the *z*-axis of the scanner, and when the length of the lead is in the range of one-quarter to one-half of the wavelength of the B_1 field, causing the formation of standing waves [13][23]. The wavelength depends on the Larmor frequency, which is determined by static field strength of the scanner ($\omega = 63.87$ MHz for 1.5T) and the relative permittivity of the tissue (ε_r) in which the lead is located, Eq. 2.9 [13].

$$\lambda_{\frac{1}{2}} = \frac{c}{2 \cdot \omega \cdot \sqrt{\varepsilon_r}} \text{ and } \lambda_{\frac{1}{4}} = \frac{c}{4 \cdot \omega \cdot \sqrt{\varepsilon_r}} \tag{2.9}$$

By assuming a conservative scenario with a background medium of water ($\varepsilon_\mathrm{water} = 84.6$), this amounts to a lead length of 13 to 26 centimetres. This corresponds to the lead lengths of the AIMD in this research. Therefore, it can be expected that heating around the AIMD will occur mainly at the ends of the lead due to the antenna effect. Also, heating will be most prominent if the lead is oriented along the *z*-axis of the scanner.

2.3 Gradient Field (G)

With the B_0 and B_1 fields, it is possible to create a signal that differentiates tissues. However, with only these two fields, no spatial information can be obtained about origin of the signal. For spatial encoding of the signal the gradient field (G), is introduced. The gradient field introduces slice, frequency and phase encoding allowing three-dimensional localisation of the signal. These three encoding mechanisms function through a gradient field that superimposes a small magnetic field gradient ($\mathrm{mT/m}$) on the static magnetic field. This causes the characteristics of the spins (f, φ) to change slightly along the direction of the gradient, allowing excitation of specific slices and identification of the origin of the signal in the transverse plane during reception of the signal [12].

The two potential hazards connected with the gradient field, gradient induced heating and vibrations, stem from the interaction of the switching gradient fields with the major conductive surfaces of an AIMD. These mechanisms are mainly dependent on the magnitude of the alternating gradient field and originate from eddy currents in the conductive surfaces of the AIMD [13][23]. The deposition of energy by the eddy currents is confined within the conductive surfaces but may diffuse into adjacent tissue [23]. This predominantly occurs in implants with large conductive surfaces where large closed current pathways can develop [23]. This effect is minimal in small implants with minimal conductive surfaces which is illustrated by the strong dependence on the dimensions of the conductive surface ($h \cdot r^4$) in Eq. 2.10 and Eq. 2.11 [11].

$$P = \sigma \cdot \pi \cdot \frac{h \cdot r^4}{8} \cdot \left(\frac{dB}{dt}\cos(\beta)\right)^2 \tag{2.10}$$

Gradient induced heating is defined in Eq. 2.10 [11] given the dimensions of the surface (h)(r), its conductivity (σ), the magnitude of the gradient field ($\frac{dB}{dt}$) and the orientation of the conductive surface with respect to the gradient field (β). Considering the AIMD of this research, the titanium enclosure of the internal magnet, although small, is the largest conductive surface. Thus, heating will mainly occur around this region. Given the dimensions of the enclosure, the conductivity of titanium and the typical gradient strength of a gradient heavy sequence (EPI), the expected gradient induced heating can be approximated to be 31.6 μW. In context of a 30 minute EPI scan protocol, this corresponds to heating of approximately 0.15 degrees Celsius at maximum. Although the expected gradient induced heating is much lower than the expected RF induced heating, the same safety limit (section 2.2) will be used for both mechanisms.

$$\tau_g = \frac{1}{8} \cdot \sigma \cdot \pi \cdot h \cdot r^4 \cdot \left(B_0 \cdot \frac{dB}{dt}\sin(\alpha)\cos(\beta)\right) \tag{2.11}$$

Gradient induced vibration is defined as the torque that is exerted on the conductive surfaces as a result of the switching gradient fields and is defined in Eq. 2.11 [11] for the static magnetic field strength (B_0) and the orientation of the magnetic moment induced by the eddy currents with respect to the static magnetic field (α). Again, an approximation can be made on the torque that is induced by the gradient fields. This will amount to roughly 237 μNm. The exact torque acting on the device due to the alternating gradient fields was not determined experimentally but the vibrations that are induced may cause dysfunctionality of the device which was assessed.

2.4 Safety Limits

A set of safety limits have emerged from the previous sections on the interactions of the AIMD with the various electromagnetic fields of the MRI scanner. These safety limits are summarised in Table 3 in order of appearance in the ISO/TS 10974 and were used as a benchmark throughout this research.

Table 3 Summary of the safety limits to which the experimental results will be compared

Hazard Mechanism	**ISO clause**	**Safety limit**			**Source**
RF induced heating	8	ΔT < 0.85 °C	OR	CEM43 < 21	[24][25]
Gradient induced heating	9	ΔT < 0.85 °C	OR	CEM43 < 21	[24][25]
Gradient induced vibrations	10	Device remains functional			[11]
B_0 induced force	11	$F \leq 1.8$ N [1]			[26]
B_0 induced torque	12	$\tau \leq 0.043$ Nm [2]	OR	$F \leq 5$ N [3]	[27][26]
B_0 induced demagnetisation	N.A.	Unknown			
Combined Fields test	17	Device remains functional			[11]

[1] *Comparison to the current generation of Cochlear Implants*
[2] *Maximal torque found for a current generation CI with a rotatable magnet*
[3] *Comparison to older generations of Cochlear Implants with an axial magnet*

3. Methods

3.1 Static Magnetic Field (B_0)

3.1.1 B_0-induced translational force

This test method is based on ISO/TS 10974:2018 clause 11, ASTM F2052 and Stoianovici et. al [11][28][29]. It defines a method to measure the translational force exerted on the AIMD by the spatial gradient of the static magnetic field (∇B_0) and compare it to the ordinary gravitational forces to which the AIMD is subjected normally.

To measure the magnetically induced translational force, the implant was attached to the test fixture shown in Figure 4. This setup was designed by Stoianovici et. al. [29] according to the requirements of ASTM F2052 [28]. The test fixture was constructed from MR compatible materials and was capable of retaining the tested AIMD without the fixture itself deflecting in the direction of the magnetic field (section 6.1 [28]). Adjustments have been made to ease the construction process. The baseplate (r = 150 mm) is cut out of 5 mm thick plexiglass. On this, a knob was placed in the centre around which the setup could rotate. A set of screw holes have been made in the baseplate of the test fixture through which the setup was attached to an in-house made mount that can be fixed to the table of the MRI scanner to ensure proper safety of the test fixture. For this, nylon M6 screws were used. Another screw hole was made in the centre of the baseplate so that the test fixture can be attached to the baseplate for extra safety. The bottom and top cross were 3D printed using a FormLabs printer with FormLabs Resin Tough 1500. The bottom cross was tapped M8 to allow for a brass M8 threaded rod to be anchored in it. Even though brass is considered MR conditional, these rods were necessary to ensure rigidity of the setup and prevent it from deflecting. The top cross is supported by the threated rods on which nylon M8 bolts were placed to fix the position of the cross. The vertical position of the top cross can be varied by rotating the bolts. The vertical angle protractor used for measurement of the deflection was 3D printed and secured using nylon M4 screws. The AIMD was attached to the test fixture with a 3D printed mount and flexible string lock (FormLabs Elastic 50A resin) so that it was hanging vertically in the zero position of the angle protractor. For this, nylon string was used. To be able to neglect the weight of the string relative to the AIMD, it has been specified that the weight of the string should not exceed 1 percent of the weight of the AIMD (section 6.1 [28]). Only 0.02 grams (0.5%) of nylon string were attached to the AIMD which complies with the requirement.

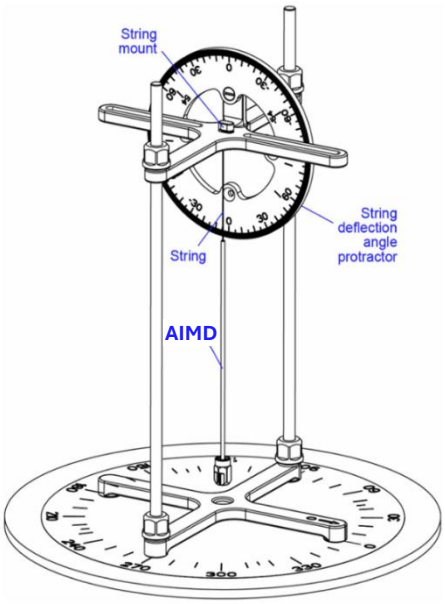

Figure 4 ASTM F2025 inspired force measurement test fixture [29]

The test fixture was positioned so that the centre of mass of the fixture was located at the position of maximum deflection. That is to say, the location at which the spatial gradient of the static magnetic field is the greatest. This location is for most MRI-systems near the opening of the bore and was identified by moving the test fixture across the surface of the patient table while searching for the position that resulted in maximal deflection of the AIMD. All tests were conducted at this location (section 8.1 [28]). The device was held so that the string was in the zero

position (0°) and then released to analyse the deflection of the device θ with respect to the zero position. Measurements were rounded to the nearest degree and repeated three times (section 8.1 [28]). In case the deflection was of such magnitude that it approaches an angle of 90 degrees with respect to the zero position, extra weight was added to the AIMD in order to obtain a measurement. This additional weight was included in the total mass ($m_{total} = m_{implant} + m_{additional}$) when calculating the displacement force [26]. The experiment was also repeated for the AIMD with the internal magnet removed to analyse the attractive force on the other components of the AIMD.

Given the mean displacement (θ) averaged over all individual measurements, the force induced by the static magnetic field was calculated according to Eq. 3.1 (section 9.2 [28]).

$$F_m = mg \cdot \tan(\theta) \tag{3.1}$$

The magnetically induced force was compared to the gravitational force, Eq. 12 [28].

$$F_g = mg \tag{3.2}$$

Acceptance criteria are met if theta is less than or equal to 45 degrees (section 9.2 [28]). A deflection of less than 45 degrees implies that the magnetically induced force (F_m) is less than the gravitational force acting on the AIMD. However, since the magnetically induced force exceeded the gravitational force, a comparison was made with respect to the forces acting on MR compatible Cochlear Implants.

3.1.2 B_0-induced torque

This test method is based on ISO/TS 10974:2018 clause 12, Stoianovici et. al., and ASTM F2213 [11][29][30]. It defines a method to measure the torque exerted on the AIMD induced by the static magnetic field gradients (B_0) and compare it to the gravitational torque to which the AIMD is subjected on a daily basis. ASTM F2213 (section 7. [30]) defines the five test methods shown in Table 4. These methods pose a number of problems with regards to the AIMD that is the focus of this research which are specified in Table 3.

Table 4 ASTM F2213 methods to measure magnetically induced torque and the problem with the tested AIMD [30]

Method	***Problem***
1. Low friction method	Requires to surface of the AIMD to be even
2. Torsional spring method	Difficult to obtain an MR-safe torsional spring
3. Pully method	Introduces friction complicating the measurement
4. Suspension method	Indicative test, requires (2) or (3) to calculate exact torque
5. Calculation method	Complex and difficult to achieve a reasonable accuracy

Method (2) appears to be the most appropriate way to determine torque. However, it is difficult to obtain an MR Safe torsional spring with an appropriate stiffness and a maximum displacement that complies with the ASTM [30]. ASTM F2213 prescribes a maximal torsional displacement of 25 degrees with respect to the zero position (section 7.5.1.5. [30]). Although Stoianovici et. al. offers an approach that circumvents the need for a torsional spring by combining methods (2) and (3), this approach proved unsuitable after an initial experiment because the AIMD aligned completely with the magnetic field. Thus, ASTM method (2) was revisited and the test fixture was modified so that a torsional spring could be implemented. The AIMD was placed vertically in the 3D printed (FormLabs Resin Though 1500) holding platform (1) and secured with a tie wrap, see Figure 5. This platform was suspended by 5 centimetres of nylon trimmer line (d = 3 mm) at each side. The trimmer line was secured to the platform using the pressure of nylon M4 screws. On the opposite end, the trimmer line is secured through two additional printed parts (2) and (3), again using M4 screws to fix the trimmer line. It is important that the holding basket is fixated in such a way that it aligns with zero degrees on the angle protractor. The trimmer line acted as a torsional spring and the magnetically induced torque was calculated with the mechanical properties of the nylon trimmer line and the deflection angle.

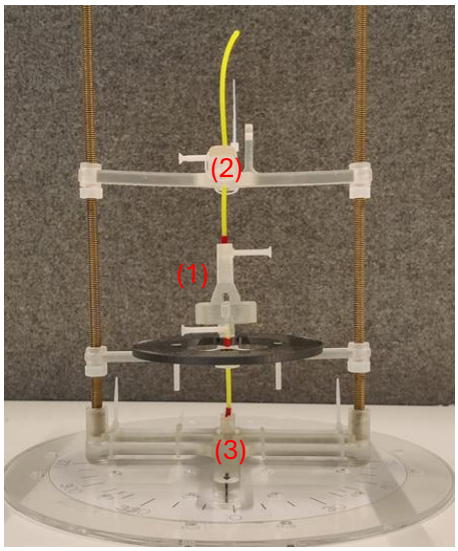

Figure 5 Test fixture for magnetically induced torque based on ASTM F2213 method (2)

The test fixture was positioned at the isocentre of the bore of the MR scanner to ensure maximum uniformity of the static magnetic field (B_0). The test fixture was then rotated on the base plate for 0 to 360 degrees with increments of 10 degrees (section 8.1. [30]). The baseplate angle corresponds to the orientation of the patient with respect to the z-axis of the scanner. Thus, the orientations of 0 and 180 degrees represent the clinically relevant feet- and head first positions. The deflection angle (θ) was measured on both sides of the protractor, averaged and converted to a torque-value. The experiment was conducted at the scanner isocentre and at the location corresponding to a knee acquisition, 106 centimetres from the isocentre (Table 15, section 17.2. [11]). The torque in the isocentre was also considered for an AIMD with the internal magnet removed. According to ASTM 2213, the magnetically induced torque can be calculated with Eq.

3.3 (section 7.5.2.4. [30]). Herein, θ is the experimentally determined deflection angle and k the torsional spring constant.

$$\tau_m = k \cdot \theta \tag{3.3}$$

To determine the magnetically induced torque, the torsional spring constant of the nylon trimmer line must be determined using Eq. 3.4 [31][32]. Herein, G is the shear modulus of the nylon line, J the polar moment of inertia of the line and L the length of the line.

$$k = \frac{G \cdot J}{L} \tag{3.4}$$

The shear modulus of a line can be estimated through experimental determination of the Young's modulus (E) and the Poisson Ratio (v). Eq. 3.5 [31][32] can then be used to calculate the shear modulus. The polar moment of inertia can be calculated with the diameter of the line (d) and Eq. 3.6 [32].

$$G = \frac{E}{2(1+v)} \tag{3.5}$$

$$J = \frac{\pi \cdot d^4}{32} \tag{3.6}$$

Estimating the exact torque is complicated because it requires the Young's Modulus and Poisson Ratio which are difficult to determine for a thin nylon line. Because of this, a torque range based on the range of the material properties of nylon was established [33]. It was decided to validate the theoretical approach by recording the deflection angles in the MRI environment and then using a force meter (Mecmasin ELS250N) outside the MRI scanner to measure the force required to pull the platform to the same angle. Then, using this measured force (F), the arm (r) and the geometry of the test setup, the torque was determined using Eq. 3.7 [26]. The setup shown in Figure 6 was used in which the original setup was flipped to a horizontal position. Bearings were used at both supports closest to the rotating platform to minimize the effect of resistive forces on the measurement.

$$\tau_m = F \cdot r \tag{3.7}$$

According to ASTM F2213 section 5.3 [30], an AIMD is considered safe if the magnetically induced torque is less than or equal to the gravitational torque. However, since the magnetically induced torque exceeded the gravitational force significantly, a comparison was made with respect to the torques acting on Cochlear Implants with MR compatibility labelling. Because the magnetically induced torque was significantly larger than the gravitational torque, the torques were compared to the rotational forces acting on MR compatible CIs.

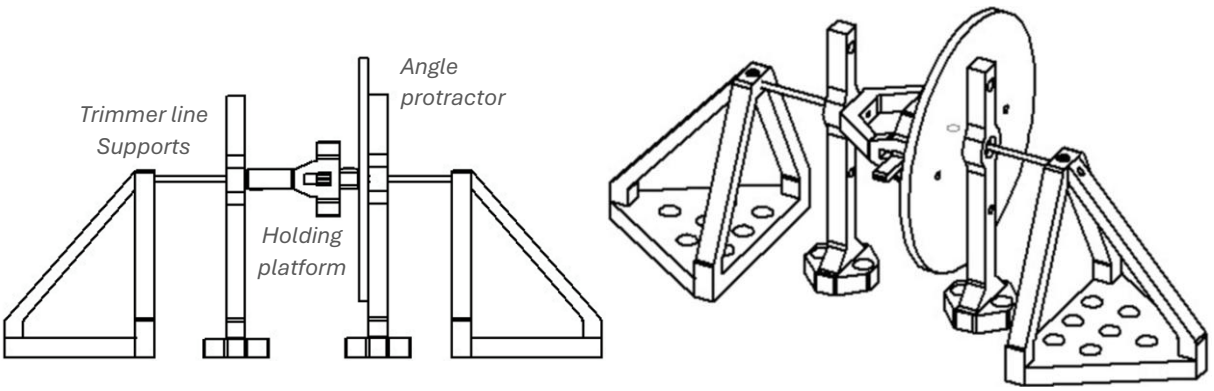

Figure 6 Visualisation of the torque verification setup. The original torque setup was flipped horizontally to be able to use the vertical force meter.

3.1.3 B_0-induced demagnetisation

The static magnetic field (B_0) of the MRI scanner may cause demagnetisation of the AIMD's internal magnet which could lead to potential failure of the transcutaneous coupling between the implant and the external stimulator. There is no specific standard that outlines a method for the measurement of demagnetisation given that demagnetisation does not pose an immediate threat to the patient. Hence, this test method was based on the papers by Majdani et. al and Dubrulle et. al. [21][22].

The test fixture was 3D printed with PLA and is meant to keep the magnets in position. Similar to Dubrulle et. al [22] , magnets were oriented in the range of -30 to 30 degrees with respect to the *z*-axis of the MRI scanner using 5-degree increments. This range covers the full range of possible orientations of the head towards the right and left shoulder within a conventional horizontal bore MRI system. To cover the opposite orientations (150° to 210°), another set of magnets was inserted into the test fixture with opposite orientation (by flipping the poles of the magnet).

The test fixture is meant to position the magnets in different orientations with respect to the static magnetic field (B_0) of the MRI scanner. The magnets were placed in their respective capsules (dimensions: 7.30 x 2.80 mm). Next to the magnet capsule is a cavity that allows for insertion of the axial probe of the Gauss meter (dimensions: 5.30 x 1.90 mm). This enabled consistent measurements of the magnetic field strength while keeping the magnets in the test fixture. The magnetic field strength of the 26 neodymium magnet samples was measured. To analyse the effect of different orientation angles on demagnetisation, it is important to verify that all tested samples have a similar initial magnetisation. After selecting 26 suitable magnets, the magnets were placed in the bottom of the test fixture after which the top of the test fixture was placed and fastened with 4 nylon screws. A 3D model of the test setup is given in Figure 7. A Gauss meter (Project Elektronik) with the AS-NTM-2 transverse probe was used to record the initial magnetization of the 26 sample magnets. The Gauss meter was set to DC measuring mode and measuring range B3. The test fixture was secured to the patient table using straps and sandbags and slid into the isocentre of the MRI bore for at least 1 second. This duration is long enough to have any potential demagnetisation occur and stabilize [21].

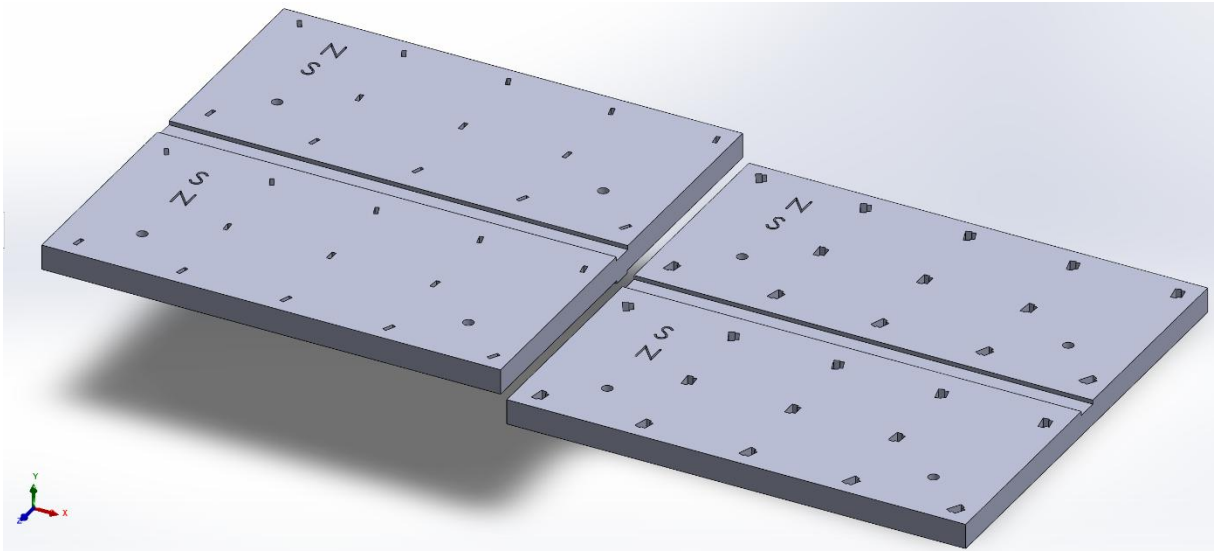

Figure 7 CAD model of the demagnetisation test fixture holding 26 magnets. Dimensions: 220 x 220 mm

Demagnetisation was tested in three MR-systems; (1) Siemens Magnetom Aera 1.5T, (2) Philips Achieva TX 3.0T and (3) Philips Achieva 7.0T. For the 7.0T system, only four orientations were analysed due to strong translational and rotational forces acting on the test fixture. Due to time constraints, only one set of four orientations could be tested. Also, this field strength is less relevant as 7.0T scanners are rarely used for clinical applications. The magnetisation of the neodymium magnets was measured after each exposure for a maximum of 10 exposures. Demagnetisation is determined by comparing the magnetic field strength after exposure with the initial magnetic field strength using Eq. 3.9.

$$(De)magnetization\ (\%) = \frac{M_{exposed} - M_{initial}}{M_{initial}} * 100 \quad (3.9)$$

3.2 Radiofrequency Field (B_1)

This test method is based on ISO/TS 10974:2018 clause 8 [11]. The standard outlines a comprehensive approach for verification of RF-induced heating. This four-tiered approach describes four, in difficulty increasing, methods to approach RF heating. In this research, a simplified Tier 3 approach was used in which a computer simulation was first conducted to determine the hotspots of the AIMD. The simulation was then validated in vitro in an MRI scanner through measurement of the actual heating around the hotspots with temperature probes.

3.2.1 ASTM Phantom

Some experiments were performed in a standardised phantom, roughly the shape of a human torso. This approximates the situation with a patient inside the scanner as closely as possible. This is important for simulating the right RF load, for example, as the scanner tunes this to the characteristics of the patient or phantom inside the scanner (section 8.1 [34]).

The phantom was designed using 10 millimetre thick polypropylene sheets according to the dimensions provided in ASTM F2182 (section 8.1 [34]). An outline of this phantom is shown in Figure 8. The ISO/TS 10974:2018 specifies that tests should be performed with the AIMD placed in a tissue simulating medium, in this case a High Permittivity Medium (HPM) (section 17.3 [11]). Hydroxyethyl Cellulose (HEC) gel (3%) was used to approximate the electrical properties of the scalp and the water which was used in the simulation step. Given that a sufficient amount of HEC to fill the entire phantom was not at our disposal, it was chosen to fill a plastic container (390x100x110 millimetres) with HEC to a depth of ten centimetres (section 8.1 [34]). The AIMD was placed in the container and mounted on a grid to suspend the AIMD and to retain its position along the *z*-axis and at a central depth within the HPM (section 17.3 [11]). The plastic container with the AIMD was placed in the head compartment of the phantom. Next, the phantom was placed on the patient table of the MRI scanner and the remaining volume was filled with a NaCl-solution (2.25 g/L) to approximate the situation of a completely HPM-filled phantom as closely as possible.

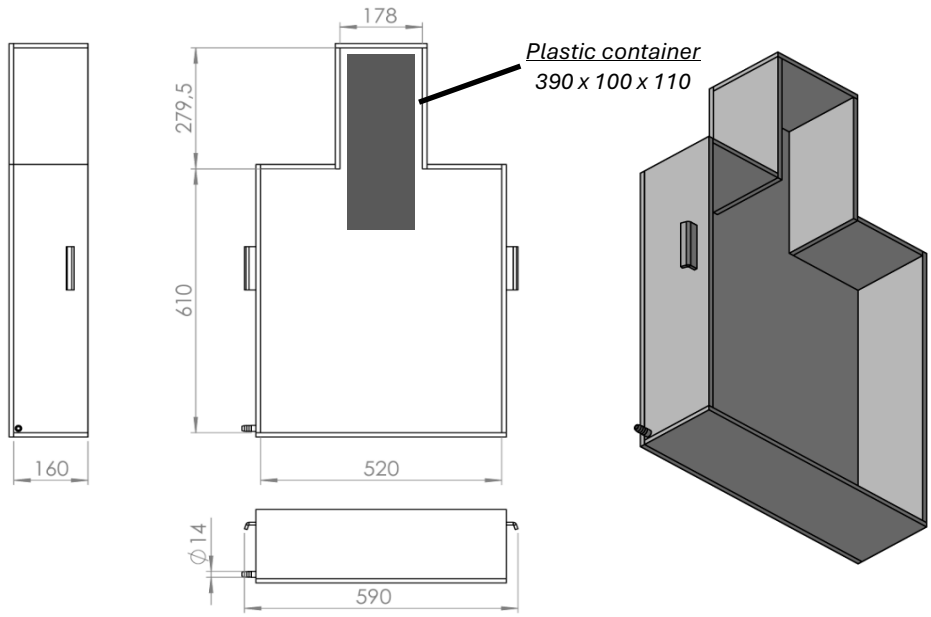

Figure 8 Visualisation of the ASTM phantom and the plastic container. All dimensions are given in millimetres

This phantom was used in the RF (3.2.3) and Gradient (3.3.3) heating experiments and in the Combined Fields Test (3.4). In these chapters, it will be referenced as the ASTM phantom.

3.2.2 Simulation of RF heating

The program CST Studio Suite (Dassault Systems, Providence Rhode Island, USA, version 2024) was used for simulating the RF induced heating around the AIMD. In this simulation, an ASTM phantom filled with water was placed in an MRI RF body transmit coil, see Figure 9. An accurate CAD model of the AIMD with appropriate material properties was placed in the ASTM phantom. Then, simulations were run in which the RF fields of a 1.5T MRI scanner and the interactions with the AIMD were simulated. From this, results showing the RF field distribution (B_1), the heating rate (SAR) and the current density in the volume of the phantom were generated. These results were used for identification of the hotspots that will be validated in-vitro. In addition to the situation shown in Figure 9 where the AIMD is positioned along the *z*-axis of the scanner (worst-case) simulations were also run for the situation in which the AIMD would be positioned along the *x*-axis of the scanner. This was done to assess the orientational dependence of the RF induced heating.

The AIMD was placed in a water-filled phantom to approximate the tissue characteristics of the location of implantation in the head. This was done because water as a medium provides a conservative approach to RF induced heating by maximizing the antenna effect considering the Larmor frequency of a 1.5T system ($\omega = 63.87$ MHz). This is due to the relatively high permittivity (78) and conductivity (1.59 $\mathrm{S/m}$) of water in comparison to most tissues. Consequently, the simulation will overestimate the RF absorption around the AIMD, allowing a safety margin with respect to the actual situation. Also, the simulation does not consider any natural cooling mechanisms such as blood perfusion. This also results in overestimation of the induced heating.

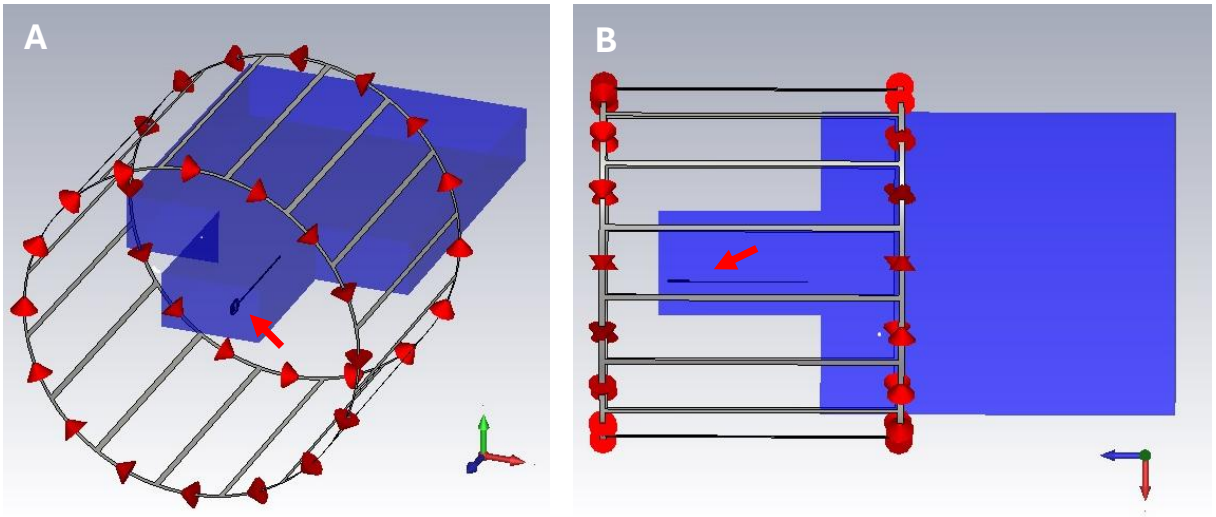

Figure 9 A) Side view of the simulation setup. B) Top view of the simulation setup. The red arrows show the location of the AIMD

3.2.3 In-vitro validation RF heating

This test method is an approximation of the protocol explained in clause 8.8 of ISO/TS 10974:2018 [11]. According to the theory of the antenna effect and the simulation in CST Studio Suite, RF induced heating is anticipated predominantly at the end of the lead, i.e. around the eighth, most distal, electrode. The AIMD was placed inside the ASTM phantom which was moved towards the isocentre of the scanner. To measure the change in temperature, a fibre optic temperature probe (OpSens Medical) was positioned in front of the eighth electrode AIMD. An additional fibre optic temperature probe was positioned near the edge of the ASTM phantom to measure the ambient temperature (section 9.3.5. [11]). These probes were connected to a signal conditioner (OpSens Medical - TempSens) outside the MRI room that was connected to a PC where the data was registered in the SoftSens software. The setup in shown in Figure 10.

To maximise the amount of RF induced heating, an RF-heavy Fast Spin Echo (FSE) sequence was used. Sequence parameters were optimised to achieve a head SAR of 99.0 percent (avg. RF power: 160 W). This was equal to a body SAR of 87.0 percent (avg. RF power: 208 W) for the measurement performed in the torso compartment. The difference in the SAR is due to the fact that the AIMD does not fit transversely in the head of the phantom. Consequently, in order to analyse the effect of the orientation on RF induced heating, the AIMD had to be placed in the torso of the phantom which changed the RF load because of the difference in patient volume inside the scanner. The SAR of the body acquisition was not changed because it was tuned to the head acquisition and the goal was to measure the SAR in the head compartment. An overview of the sequence parameters is given in Table 5. This scan protocol was executed for a duration of six minutes (section 201.12.4.103.2 [24]). Measurements were done twice, after which the AIMD was repositioned in the torso of the ASTM phantom and oriented along the *x*-axis of the scanner. Care was taken to ensure that although in a different position in the ASTM phantom, the AIMD was in the same position along the *z*-axis with respect to the isocentre of the scanner. The experiment was conducted in a similar manner for this position. The temperature data was organised and plotted with a MATLAB® (MathWorks, Natick Massachusetts, USA, version R2024b) script. Another MATLAB® script was used to determine the corresponding CEM43 values.

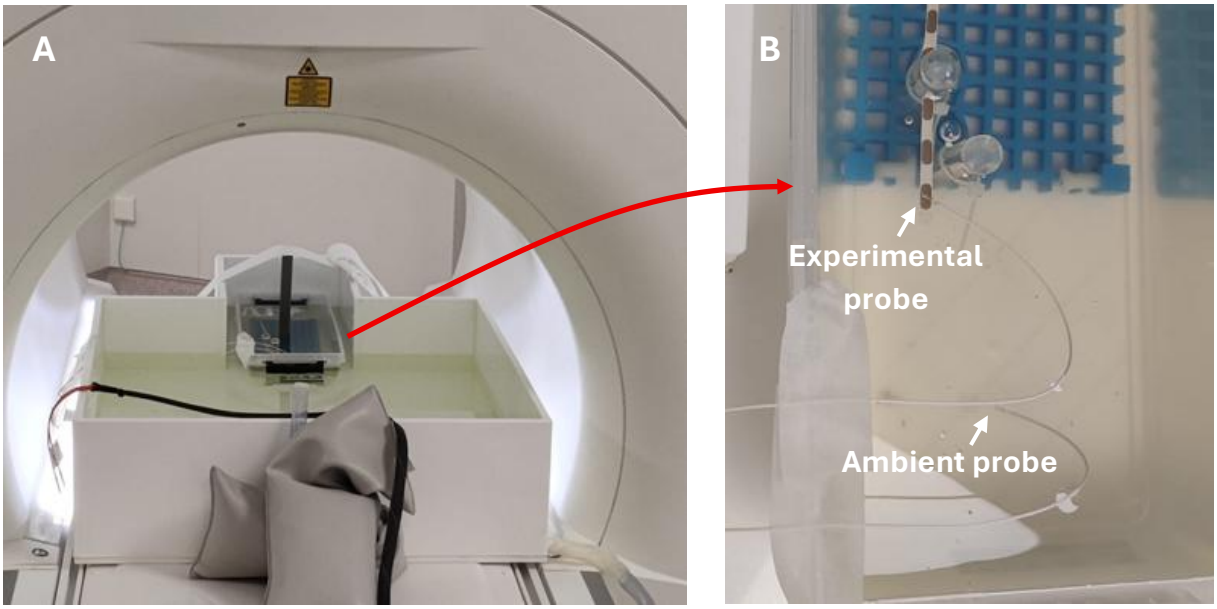

Figure 10 RF induced heating setup with the experimental probe near the eighth electrode of the lead and the ambient probe near the edge of the phantom container

Table 5 FSE (max SAR) sequence parameters used in the RF induced heating experiment

Sequence	*Fast Spin Echo (FSE) - Max SAR*
T_R	1760 ms
T_E	84 ms
Flip angle	175
Averages	1
Turbo factor	192
Echo spacing	3.66 ms
Echo train duration	432 ms
Bandwith	574 Hz/px
RF pulse type	Fast
Slice thickness	1 mm
Matrix size	256 x 256 mm
FoV	256 x 256 mm
Phase Encoding dir.	Right >> left

3.3 Gradient field (G)

3.3.1 Validation of gradient field strength

To comply with the standard, it is mandatory to prove that the AIMD was exposed to sufficiently strong gradient fields for both the gradient vibration test $(dB/dt)_{peak}$ and the gradient induced heating experiment $(dB/dt)_{RMS}$. For this, a search coil was designed. This search coil was designed according to IEC 60601-2-33 (section 201.12.4.105.2.2b, [24]). The copper coil has 55 turns (n) and an inner diameter of 48 mm ($r = 24\ mm$). Given these properties, Eq. 3.10 [24] can be used to calculate the (dB/dt)-levels based on the voltages that are induced in the coil by switching of the gradients.

$$\left|\frac{dB}{dt}\right| = \left|\frac{V_{coil}}{n\pi r^2}\right| \tag{3.10}$$

To validate that the AIMD was exposed to the proper $(dB/dt)_{peak}$-levels during the gradient vibration experiment, the search coil was placed 10 centimetres along the *x*-axis from the isocentre of the scanner, see Figure 11. A $CuSo_4$-filled phantom was placed near the isocentre of the scanner to ensure that the scanner is able to calibrate and initiate scanning. Subsequently, measurements were performed with the search coil oriented along all three axis (x,y,z) of the scanner where transverse, sagittal and coronal scan directions were measured for each orientation. Finally, measurements were performed in which the search coil was placed in the same orientations as mentioned previously but in this case with the search coil moved another 30 centimetres along the *z*-axis with respect to the isocentre of the scanner. This was done because a larger deviation from the isocentre (*z*-axis) will cause the root mean square value of the gradients $(dB/dt)_{RMS}$ to increase [23]. The search coil was connected to a oscilloscope (Tektronix DS2014C) with a COA*X*-cable. Data was saved from the oscilloscope using a USB-drive. A MATLAB® script was used to analyse this data. The script determines and plots the (dB/dt)-values from the induced voltage in the search coil, identifies the $(dB/dt)_{peak}$-values and calculates the $(dB/dt)_{RMS}$-values. The (dB/dt)-values obtained using Eq. 3.10 are converted to a $(dB/dt)_{RMS}$-value using Eq. 3.11 [11].

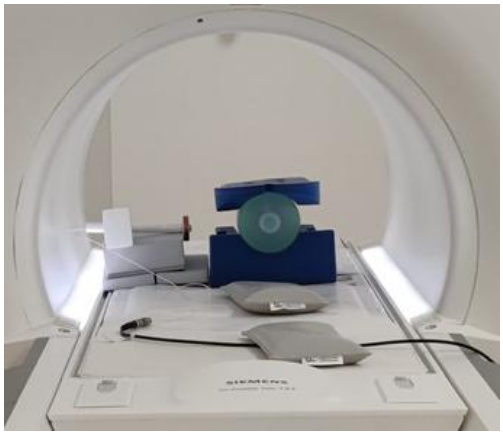

Figure 11 Experimental setup for determination of the dB_x/dt levels. The search coil is oriented along the x-axis of the scanner. The $CuSO_4$ phantom is placed near the isocentre of the scanner

$$\left|\frac{dB}{dt}\right|_{RMS} = \sqrt{\frac{\int_0^{t_x}\left|\frac{dB}{dt}\right|^2 dt}{t_x}} = \sqrt{\frac{1}{N_m}\sum_{i=1}^{N_m}\left(\frac{V_i}{N_m\pi r^2}\right)} \tag{3.11}$$

In order to meet the requirements of the ISO/TS 10974:2018, a scan sequence must be identified that produces $(dB/dt)_{peak}$-values greater than 63.7 T/s (section A.2.2, Table A.2, [11]) and $(dB/dt)_{RMS}$-values greater than 29.8 T/s (section 9.2.2., Table 5 [11]). It is recommended to use an Echo Planar Imaging (EPI) sequence to achieve the correct (dB/dt)-level (section 10.3.5.2. [11]). Several EPI sequences were tested to identify the scan protocol that maximizes (dB/dt)-levels. The EPI scan protocol that was used in the experiment is provided in Table 6.

Table 6 EPI sequence parameters used in the gradient induced vibration and heating experiments

Sequence	*Echo Planar Imaging (EPI)*
T_R	153 ms
T_E	97 ms
Averages	32
EPI factor	192
Echo spacing	0.98 ms
Bandwith	1132 Hz/px
Gradient mode	Fast
Slice thickness	5 mm
Matrix size	192 x 192 mm
FoV	230 x 230 mm
Phase Encoding dir.	Anterior >> posterior

3.3.2 Gradient induced vibration

This test method is based on ISO/TS 10974:2018 clause 10 [11]. It defines a method to assess the impact of gradient induced vibration on the AIMD. The pulsed magnetic field gradients can induce eddy currents in the conductive surfaces of an AIMD resulting in a time varying magnetic moment interacting with the static magnetic field (B_0). This may cause vibration of the conductive surfaces and the device [11]. The test was meant to analyse the extent to which the AIMD remained functional after prolonged exposure to the gradients during an MRI scan.

The test fixture was constructed from plexiglass (PMMA) and is meant to secure the position within the scanner, Figure 12A. This test fixture allowed the AIMD at least 0.5 millimetres of non-restricted movement in each direction (section 10.4.2.2. [11]). The test fixture consists of three parts that were fixed together with nylon screws. In order to be allowed to perform this experiment at room temperature, it must be justified that the mechanical properties (e.g. elastic modulus) of the implant do not significantly change between room- and body temperature (section 10.3.7.2. [11]). It is difficult to obtain specific data on the temperature dependence of the mechanical properties of the main components of the AIMD. However, research considering these materials in general indicates that no substantial shift in mechanical properties between room and body temperature is to be expected [35][36]. This allowed the experiment to be conducted at room temperature.

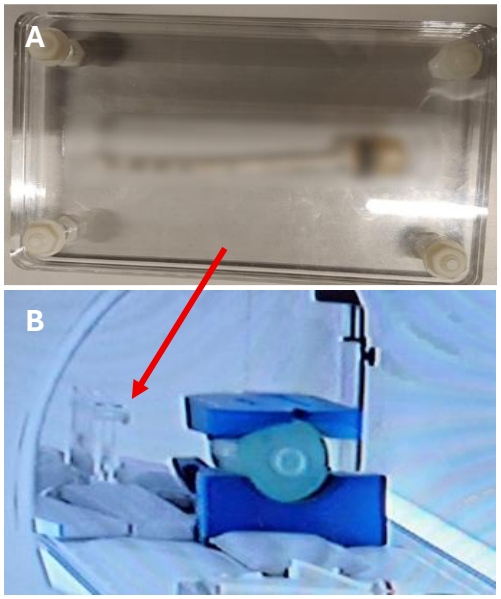

Figure 12 A) AIMD in test fixture B) Test fixture placed in MRI bore at the proper position supported with sandbags

The test fixture was positioned at the location for which the (dB/dt)-levels were verified in section 3.3.1. That is, 10 centimetres along the *x*-axis and 30 centimetres along the *z*-axis from the isocentre of the scanner, see Figure 12B. The AIMD was positioned with its major conductive planes parallel to the *z*-axis of the scanner (section 10.4.2.1. [11]). To meet the requirements of this clause, the AIMD must be exposed to a sufficient (dB/dt)-level. For this, the (dB/dt)-vector orthogonal to the major conductive planes of the AIMD (internal magnet), $(dB/dt)_x$, is important (section 10.4.1. [11]). Achieving the required $(dB/dt)_x$-level was confirmed with a gradient search coil positioned at the test fixture location in section 3.3.1. Once confirmed that the chosen sequence was in accordance with the requirements, the test was initiated. The duration of the test depends on the risk profile chosen by the AIMD manufacturer that corresponds to one of the population percentiles in Table 7. Given the exploratory nature of this research, it was chosen to comply with the 99.2th population percentile and expose the AIMD for a duration of 135 minutes (60% duty cycle) using EPI sequence for which the (dB/dt)-levels have been verified in 3.3.1. This was a standard T2-weighted EPI sequence. Sequence parameters are shown in Table 6.

Table 7 Gradient induced vibration test duration based on population percentile (%) [11]

Population percentile (%)	Test duration (h) *50% duty cycle*	Test duration (h) *60% duty cycle*
99.2	2.5	2.1
99.9	4.5	3.75
99.99	7.5	6.25

The duty cycle was defined as the percentage of the acquisition in which the gradient fields are active and was calculated in MATLAB® based on the gradient waveform acquired with the search coil.

After the prolonged exposure, the AIMD was removed from the test fixture and its functionality was tested using the external stimulator which was coupled to the AIMD. A 500 Ohm resistor circuit was placed on the sixth and seventh electrode of the lead to allow the external stimulator to conduct pre-stimulation calibration. Next, the external stimulator was turned on and its status was monitored. A green LED would indicate successful stimulation, and thus, shows that the AIMD remained functional. A blue blinking LED would indicate that the external stimulator is not able to stimulate due to an error. This would be the indicator for a dysfunctional AIMD. Inter-electrode impedances were also verified using a specially designed connector and Python® (Python Software Foundation, Wilmington, Delaware, USA, version 3) script.

Last, the internal magnet is encapsulated in a titanium housing and it is known that the magnet can loosen within the titanium housing, causing patients to hear rattling noises. To assess this issue, the AIMDs were tested for rattling after prolonged exposure during the vibration experiment in the appropriate test apparatus at the manufacturer.

3.3.3 Gradient induced heating

This test method is based on ISO/TS 10974:2018 clause 9 [11]. It defines a method to assess the gradient induced heating of the AIMD in-vitro. This was done through exposure of the device to a gradient heavy scan sequence and measuring the degree of heating.

The AIMD was placed in the centre of the HPM filled ASTM phantom given that ISO/TS 10974:2018 prescribes that the experiment must be conducted in a thermal conduction dominated environment with minimal thermal convection (section 9.3.1. [11]). The AIMD does not have a major conductive plane. The titanium enclosure of the internal magnet, although small, is the largest conductive surface which means any potential heating would probably be most evident at this location. To measure the change in temperature, a fibre optic temperature probe (OpSens Medical) was positioned near the internal magnet of the AIMD. An additional fibre optic temperature probe was positioned near the edge of the ASTM phantom to measure the ambient temperature (section 9.3.5. [11]). These probes were connected to a signal conditioner (OpSens Medical - TempSens) outside the MRI room that was connected to a PC where the data was registered in the SoftSens software. The temperature data was organised and plotted with a MATLAB® script. A setup similar to the one for the RF heating experiment shown in Figure 10 was used.

The AIMD was positioned near the isocentre, along the *z*-axis of the scanner with the magnet orthogonal to the *x*-axis. This orientation roughly corresponds to the anatomical position of the AIMD in patients. The experiment was conducted for a duration of 30 minutes. During these 30 minutes, the AIMD was exposed to the required $(dB/dt)_{RMS}$-levels. This level depends on the radial distance of the AIMD from the *z*-axis of the scanner. In this case, a distance of 10 centimetres equates to a $(dB/dt)_{RMS}$ of 29.8 T/s (section 9.2.2., Table 5 [11]). If it is not possible to expose the AIMD to the required gradient field, temperature scaling according to Eq. 3.12 [11] may be performed (section 9.3.1. [11]). To verify whether the proper $(dB/dt)_{RMS}$-levels are reached or whether temperature scaling needs to be performed a search coil was positioned at the orientation and location of the ASTM phantom as explained in section 3.3.1. For this, only the gradient component that is perpendicular to the surface of the AIMD was used, that is, $(dB/dt)_{RMS}(x)$ (section 9.3.7. [11]).

$$\Delta \mathrm{T} = \Delta \mathrm{T}_{\mathrm{measured}} \left[\frac{\left|\frac{dB}{dt}\right|_{RMS}(required}{\left|\frac{dB}{dt}\right|_{RMS}(test)} \right]^2 \tag{3.12}$$

3.4 Combined Fields Test

This test method is based on ISO/TS 10974:2018 clause 17 [11]. It defines a method to assess the in-vitro functionality of the AIMD when exposed to all three MR fields in a clinical setting. It also provides insight into the effect of acquisitions of different anatomical regions on the functionality of the AIMD rather than just head acquisitions.

The AIMD was placed in the ASTM phantom to ensure that the conditions of the experiment match the clinical reality as closely as possible. Nine clinical scans in six landmark positions with respect to the isocentre were performed. The ASTM phantom was positioned at the landmark position that corresponds to the scan that was acquired. The scanner was allowed to conduct the complete pre-scan procedure (section 17.2 [11]). Images were acquired with the whole body coil and the FoV was positioned in such a way that the *x*- and *y*-axis were centred at the phantom centre with the *z*-axis centred at the respective landmark position (section 17.2 [11]). Figure 13 illustrates the six landmark positions and the corresponding distance (cm) with respect to the isocentre of the scanner [11].

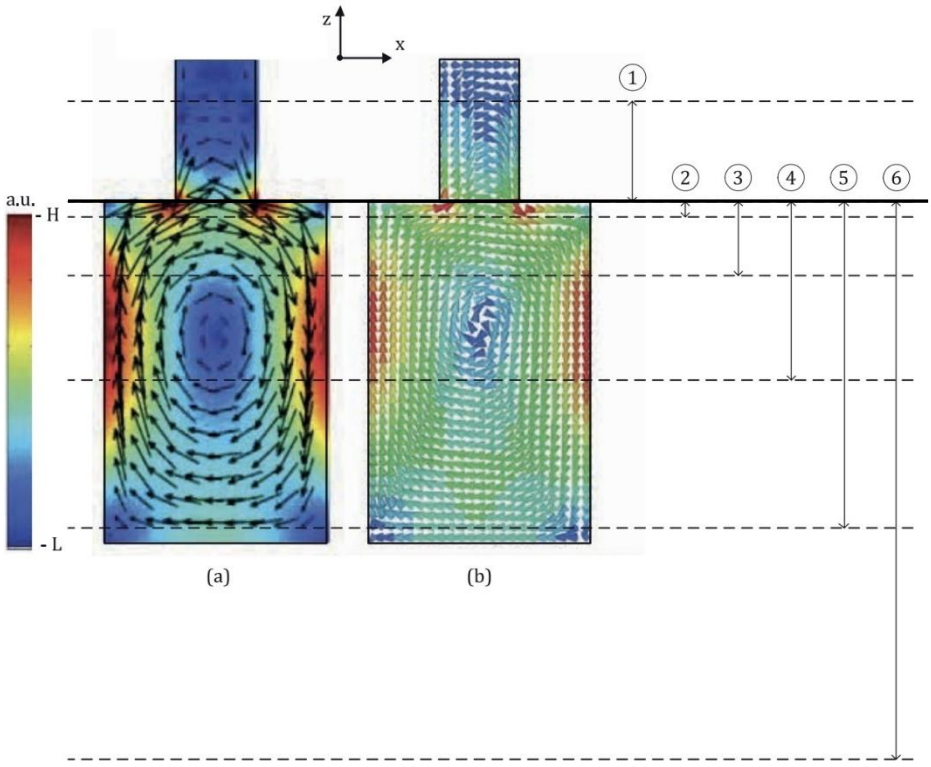

Landmark	*Position (cm)*
0	Isocentre
1	-19
2	3
3	14
4	34
5	62
6	106

Figure 13 ISO/TS 10974 specified landmarks for Combined Fields test [11]

Then, the ASTM phantom was moved to the first landmark position and the corresponding acquisition sequence as displayed in Table 8 was run (section 17.2 [11]). This table indicates the clinical sequences to which the AIMD should be subjected, the landmark at which the phantom should be placed and the minimum scan time. Measurements were repeated for nine out of 14 target regions at the correct landmark position and with the correct minimum scanning time. The other five protocols (marked red in Table 8) were not scanned due to time restrictions. However, at least one scan was completed for each anatomical landmark, and a selection of high-risk scanning procedures was chosen.

Table 8 Clinical scan protocols of the Combined Fields test and the corresponding landmark positions and minimal scan duration [11]

Protocol Target Region	Landmark Position	Minimal scan duration (min)
Neurological examinations		
Brain	1	6
Lumbar Spine	*5*	*4*
Thoracic examinations		
Liver	4	4
Kidney	*4*	*2*
MRCP	*4*	*2*
Enterography	4	2
Breast	3	2
Cardiac	3	5
Upper Limb examinations		
Hand	*5*	*3*
Shoulder	2	3
Hip examinations		
Prostate	5	3
Vulva	*5*	*5*
Lower Limb examinations		
Knee	6	2
Thigh	6	5

After each scan protocol, the AIMD was removed from the container with HPM and properly cleaned. Then, a 500 Ohm resistor circuit was placed on the sixth and seventh electrode of the lead and the external stimulator was coupled to the AIMD. The resistor circuit is required for the external stimulator to be able to conduct pre-stimulation calibration. Next, the external stimulator was turned on and its status was monitored. A green LED would indicate successful stimulation, and thus, that the AIMD remained functional. A blue blinking LED would indicate that the external stimulator is not able to stimulate due to an error. This would be the indicator for a dysfunctional AIMD. This procedure was repeated for nine scan protocols mentioned above.

3.5 Image Artifacts

This test method is based on ASTM F2119 [37]. It defines a method to measure the size of imaging artifacts that arise as a consequence of the AIMD and the internal magnet. The experiment was carried out both in-vitro and in-vivo. The in-vitro acquisition of the magnet and AIMD (without magnet) was used to determine the size of the image artifact based on the method prescribed in the ASTM F2119. The in-vivo acquisition provided an indication of the actual clinical implications of the artifact that is induced by the magnet and the AIMD.

For the in-vitro assessment, a plastic container was placed on the patient table and filled with a paramagnetic solution of copper sulphate ($CuSO_4$ [1-2 g/L]) to reduce T_1 and gain more signal (section 7.1.2. [37]). The test object (either a magnet or the AIMD) was mounted on a grid and placed at a central position in the phantom to allow for a margin between the test object and the edges of the phantom. The ASTM prescribes a margin of at least 4 centimetres to ensure adequate field homogeneity (section 7.1.2. [37]). To accurately assess the position of the AIMD in the phantom, a 3D printed PLA grid was used as a non-distortive reference object (section 7.1.3. [37]). The phantom with the test object was placed on the patient table and moved to the isocentre of the scanner. The magnet and AIMD were tested in three mutually orthogonal orientations relative to the static magnetic field (B_0) (section 7.2.2. [37]). That is, parallel to B_0 (*z*-axis) and perpendicular to B_0 considering the *x*- and *y*-axis. Then, acquisitions were made with Fast Spin Echo (FSE) and Spoiled Gradient Echo (GRE) sequences according to the parameters in Table 9 based on the recommendations in section 7.1.1. of ASTM F2119 [37]. All scans were acquired in the coronal plane to ease the analysis. Furthermore, images of the magnet acquisitions were acquired with all possible readout directions. This is recommended to evaluate the effect of the phase-encoding direction on the shape and magnitude of the artifact (section 7.2.3. [37])

Table 9 Acquisition parameters Image Artifact experiment

Sequence	*Fast Spin Echo (FSE)*	*Spoiled Gradient Echo (FL2D)*
T_R	500 ms	202 ms
T_E	22 ms	4.86 ms
Flip angle	178°	70°
dSlice	5 mm	5 mm
Matrix size	320 x 320 mm	320 x 320 mm
FoV	400 x 400 mm	400 x 400 mm

According to the definition set by the ASTM, a pixel is considered to be part of the artifact if its intensity changed at least 30 percent with respect to the reference image (section 2.1.2. [37]). The size of the artifact is given by the distance (mm) from the edge of the AIMD to the fringe of the artifact (section 7.3.1. [37]). The size of the artifact in millimetres was calculated according to Eq. 3.13 [37] and is calculated for the slice containing the artifact with the greatest magnitude. Because the AIMD itself is within the artifact and not clearly identifiable, the radius of the AIMD was subtracted from the radius of the total artifact to comply with the definition (section 7.3.1. [37]).

$$distance\ (mm) = \left(number\ of\ pixels\ \cdot \frac{FOV}{m}\right) - r_{AIMD} \tag{3.13}$$

The magnitude of the artifact was determined for both the individual magnet as well as the AIMD without magnet. Image analysis was done with a MATLAB® script that creates a mask of pixels whose intensity changed at least 30 percent and measures the size of the artifact in each direction.

Two healthy volunteers who had given informed consent participated in the in-vivo assessment. The magnet was placed in a plastic casing. This is done to ensure the safety of the test person within the high magnetic field of the MRI scanner. The 3D printed casing ensures that the magnet will stay securely in place. The encased magnet was then placed at a location on the head equal to the location of implantation and was restrained by applying bandages tightly around the head. To identify the effect of the AIMD without a magnet, the AIMD was placed on the head and wrapped with bandage. To ensure that the electrodes of the device did not come in contact with the skin it was wrapped with non-conductive plastic wrap prior to placement. It was not necessary to encase the AIMD given that the magnet was removed and the AIMD itself is of sufficient size to prevent sudden dislocation.

4. Results

4.1 Static Magnetic Field (B_0)

4.1.1 B_0-induced force

The translational force induced by the static magnetic field was analysed using the ASTM F2052 [28] inspired apparatus shown in Figure 13. It is clearly visible that the force measurement of the AIMD itself, weighing 3.8 (short) or 3.9 (long) grams, could not be used for determination of the magnetically induced force. This is due to the fact that the deflection angle approached 90 degrees preventing accurate measurement, Figure 14A. Therefore, it was decided to add weight to the samples using nylon bots or LEGO, Figure 14B. This additional weight caused the deflection angle to decrease to a measurable figure that was then be used to determine translational force. Measured deflection angles are shown in Table 10. The mean deflection angle together with the total weight of the test sample was converted to an translational force using Eq. 2.1. The magnetically induced force is compared to the gravitational force using Eq. 2.2. Results are displayed in Table 10.

Table 10 Magnetically induced translational force and its ratio with respect to gravity calculated with the measured mean deflection angles and total weight

	Mean deflection (°)	***Total weight (g)***	***Translational force (N)***	***Gravitational ratio***
1.5T	50	21.04	0.246	6.60
No magnet 1.5T	18	2.84	0.009	0.32
3.0T	55	34.93	0.489	13.13
7.0T	50	88.31	1.032	26.98

An observation is that the amount of additional weight that had to be attached to the AIMD to achieve measurable results scaled roughly with the strength of the static magnetic field (T). Consequently, the translational force and gravitational ratio also scale with the strength of the static magnetic field. It was also investigated at which position with respect to the isocentre the deflection of the implant is equal to 45 degrees implying that the magnetically induced force is equal to gravity. This was found to be that at a distance of 158 cm with respect to the isocentre. It is noticeable that the AIMD with the internal magnet removed, Figure 14C, is minimally attracted to the magnetic field, in fact even less than the gravitational force.

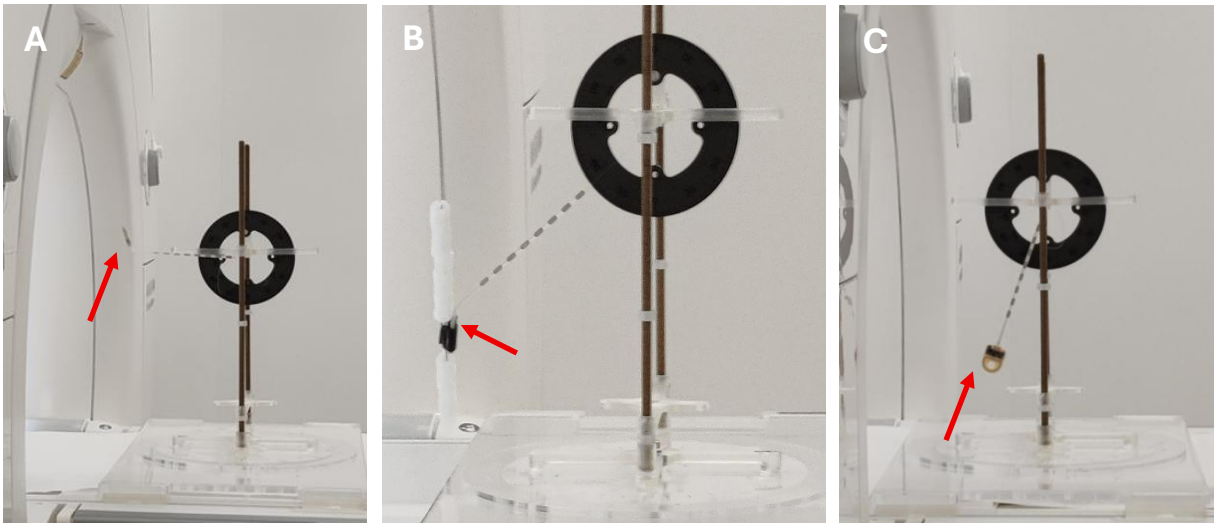

Figure 14 Deflection around the Siemens Magnetom Aera 1.5T. The red arrows indicates the stimulator unit of the AIMD. A) Maximal deflection bore entrance B) Deflection with additional weight C) Maximal deflection without the internal magnet.

The experimentally determined translational forces are well within the safety limit established through the comparison with Eerkens et. al. Therefore, the device has passed this test.

4.1.2 B_0-induced torque

The torque induced by the static magnetic field was analysed using the ASTM F2213 [30] inspired apparatus shown in Figure 15. The apparatus was positioned at the isocentre of the Siemens Magnetom Aera 1.5T and Philips Achieva TX 3.0T. For the Philips Achieva 7.0T, measurements were performed at the bore entrance because the test fixture did not fit in the smaller bore. Note that for the 3.0T and 7.0T systems, only the torque values for a baseplate angle of 0 degrees were determined due to time constraints.

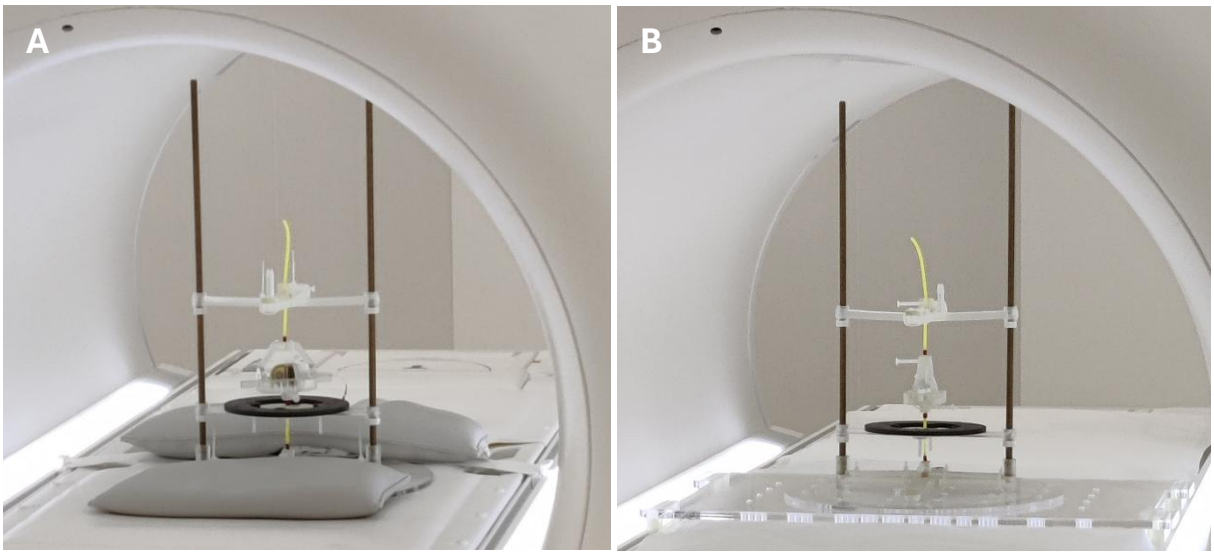

Figure 15 Both images show rotational deflections in the Siemens Magnetom Aera 1.5T system. A) AIMD with magnet showing deflection of 60 degrees at the isocentre B) AIMD without magnet showing no deflection at the isocentre.

The rotational deflection shown in Figure 15A was used to calculate the magnetically induced torque according to Eq. 3.3 – 3.6. The torque values for several orientations of the baseplate are shown in Figures 16 and 17 for the test fixture positioned at the isocentre (head acquisition) and at 106 centimetre from the isocentre (knee acquisition) respectively. The AIMD with the internal magnet removed did not show any deflection, Figure 15B.

Observing the torque at the isocentre (Figure 16), it is noticeable that the torque increases to zero as the baseplate angle aligns more with the *z*-axis of the scanner to a torque of 0 Nm when fully aligned (90°). Moving the baseplate further, causes the validated torque to increase to a maximum of 0.068 Nm at a baseplate angle of 200 degrees. For angles greater than 200 degrees, no measurement value was recorded because the deflection exceeded 90 degrees and became inaccurate. Considering the torque during a knee acquisition (Figure 17), a similar pattern is observed up to 180 degrees after which the torque increases even further up to 0.055 Nm for 260 degrees. Around 270 degrees, a clear change in the orientation of the AIMD can be seen resulting in a negative torque. The AIMD flipped to align its internal magnet with the field. Then, the torque value again builds up to zero for a baseplate angle of 90 degrees, where the internal magnet is aligned with the *z*-axis of the scanner. The torque values for an orientation of zero degrees (along the *z*-axis) for the 3.0T and 7.0T systems compared to 1.5T are shown in Table 11. It is clear that both torques are greater than the torque in a 1.5T system. There is minimal difference between the 3.0T and 7.0T systems. Here, it is important to note that the measurement for the Philips Achieva 7.0T was taken at the bore entrance rather than the isocentre.

The torque measured at the isocentre of the 1.5T system exceeds the limit set by the CI system with the rotatable magnet [27]. The torque at the knee location is also just over this limit. Thus, the AIMD is not likely to be MR conditional in terms of torque.

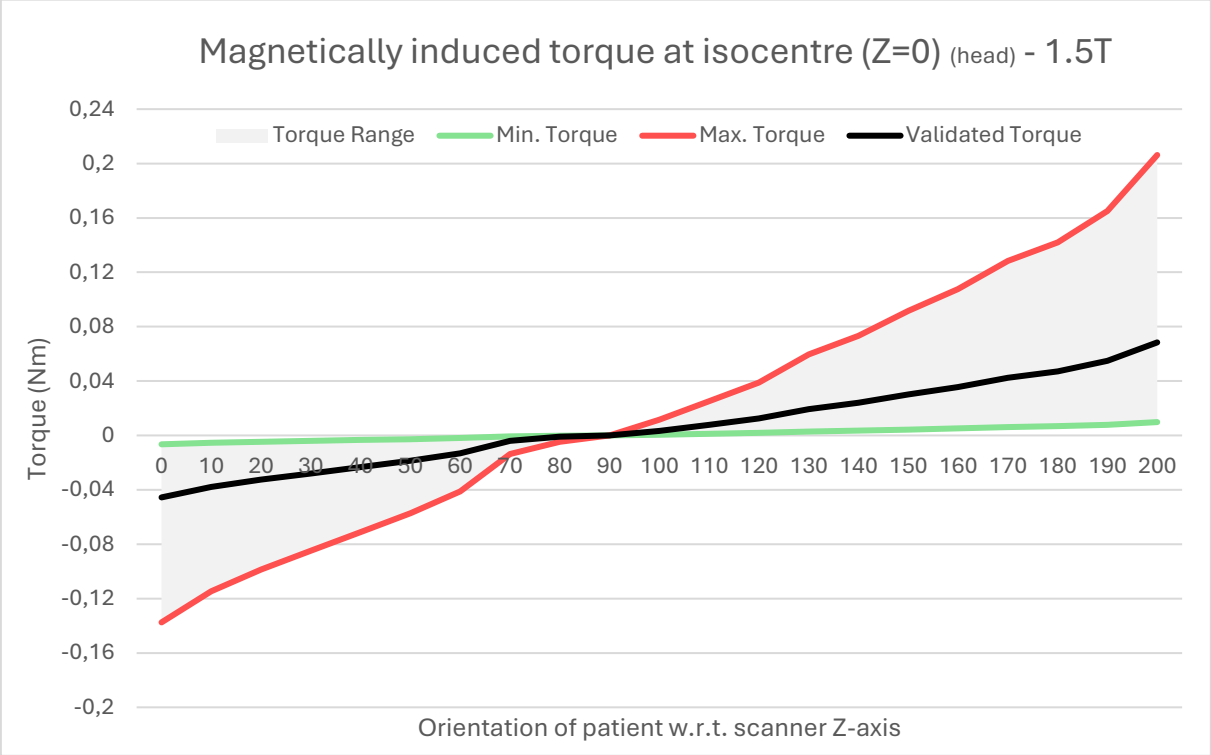

Figure 17 Theoretical torque range and validation for baseplate angles 0 - 200 degrees at the isocentre of the Siemens Magnetom Area 1.5T. This location corresponds to the location of the AIMD during a head scan.

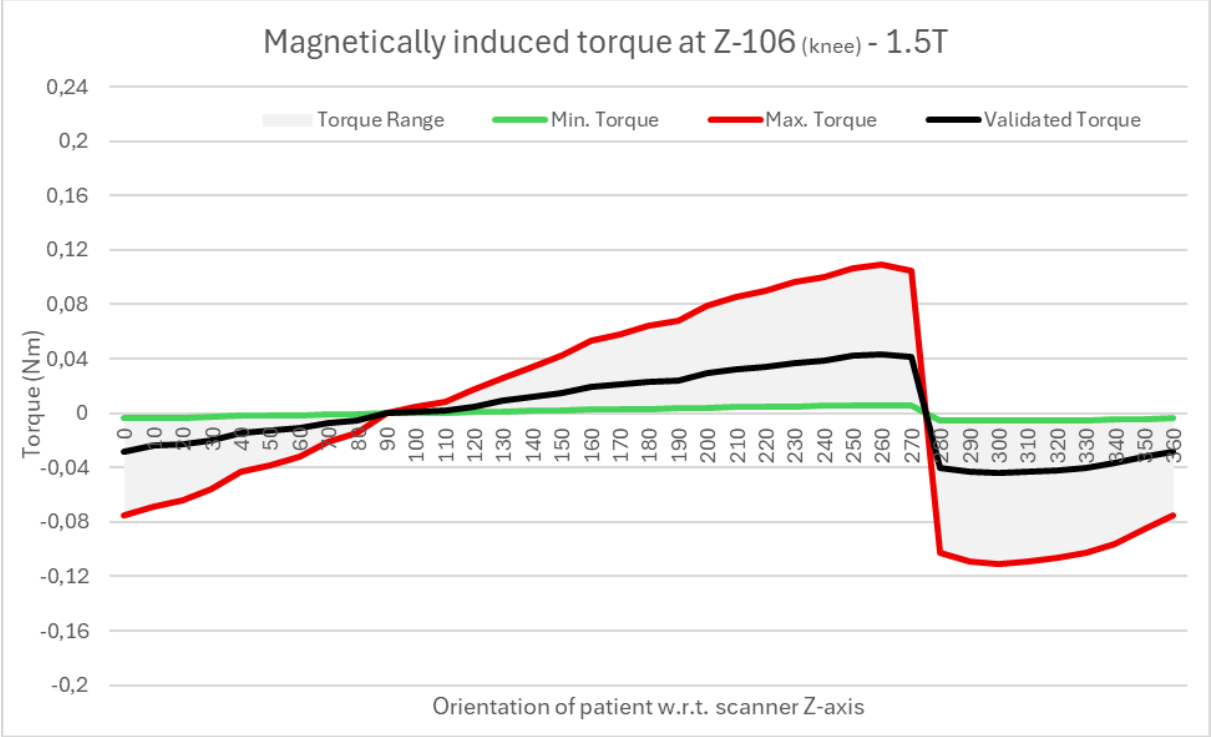

Figure 16 Theoretical torque range and validation for baseplate angles 0 – 360 degrees at 106 centimetre from the isocentre of the Siemens Magnetom Area 1.5T. This distance corresponds to the location of the AIMD during of a knee

Table 11 Torque range for all three systems at a baseplate angle of zero degrees.

	Min. Torque (Nm)	***Max. Torque (Nm)***	***Validated Torque (Nm)***
Isocentre ***1.5T***	0.006	0.137	0.046
Isocentre ***3.0T***	0.008	0.165	0.053
Bore entrance ***7.0T***	0.008	0.165	0.055

4.1.3 B_0-induced demagnetisation

The internal magnet of the AIMD was exposed to the B_0 field of three MRI scanners to determine the extent to which it demagnetises after exposure to the stronger external field. MRI scanners with three different static field strengths were used: (1) Siemens Magnetom Aera 1.5T, (2) Philips Achieva TX 3.0T and (3) Philips Achieva 7.0T. Figures 18 and 19 plot the percentual demagnetisation of the internal magnet after exposure to the external magnetic fields for the 26 orientations that were examined. It is important to note that only four internal magnets in four different orientations were exposed to the Philips Achieva 7.0T due to safety considerations.

Figure 18 shows the percentual demagnetisation of the internal magnets that were exposed to the static magnetic field of the Siemens Magnetom Area 1.5T. Magnet angles are relative to the static magnetic field of the scanner. It is clearly visible that the demagnetisation fluctuates around zero percent. The internal magnets were exposed for a total of 10 times to the static magnetic field of the scanner. All exposures were performed with an equal orientation of the test fixture. The difference between the degree of demagnetisation after one and 10 exposures is within 2.3%. This degree of variance is visible between all combinations of exposures. Although there is some degree of variation between exposures, Figure 18 shows that no major differences are observable after 5 and 10 exposures. This demonstrates that demagnetisation does not increase significantly with the number of exposures. The degree of demagnetisation induced by the static magnetic field of the 1.5T system is not thought to be harmful for the functionality of the AIMD.

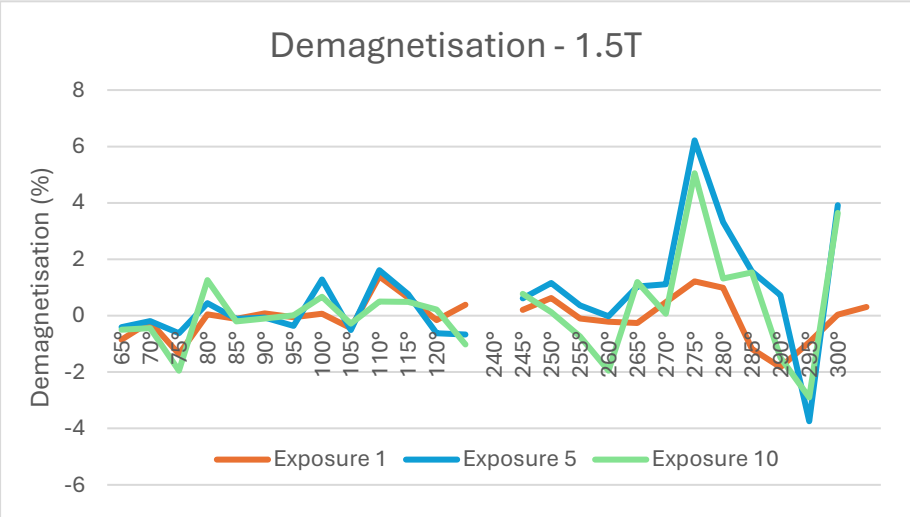

Figure 18 Demagnetisation (%) after one, five and ten exposures to a Siemens Magnetom Aera 1.5T system.

Figure 19 plots the percentual demagnetisation of the internal magnets after exposure to the static field of the Philips Achieva TX 3.0T. It can be observed easily that some internal magnets demagnetise in this stronger external magnetic field. A strong orientational dependence is observed. The least demagnetisation occurs when the magnets are roughly orthogonal to the static magnetic field, around orientations 80° and 270°. The further the orientation deviates from this, the greater demagnetisation of the magnet increases. Some internal magnets even demagnetise completely (-100 percent) or change polarisation (> -100 percent) as a result of the external magnetic field. The demagnetisation seems to be fairly stable as the number of exposures increases. Given that the demagnetisation around a 3.0T system can be quite severe (>100%), systems with this field strength are considered to be harmful for the functionality of the AIMD.

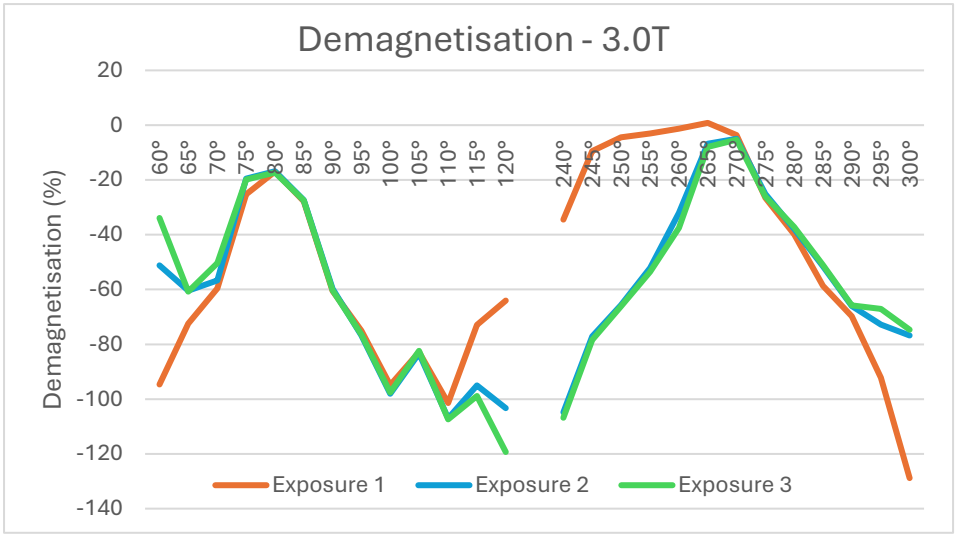

Figure 19 Demagnetisation (%) after one, two and three exposures to a Philips Achieva TX 3.0T system

Figure 20 does not show percentual demagnetisation of the internal magnets but rather the strength of the internal magnets (mT). This enables a better understanding of the effect of the static field of the Philips Achieva 7.0T while changing the orientation of the test fixture in between exposures. Although only four magnet orientations were analysed in this experiment, orientational dependency can also be observed within this small sample. Orientations 60° and 300° show an equal effect in which the external magnetic field reversed the polarisation of the internal magnet after the first exposure. A second exposure had no obvious effect on the strength of the magnet as the magnetisations remain similar. For the third exposure, the test fixture was rotated 180° so that the polarisation of the external magnetic field and the internal magnet were again oriented in opposite directions. Similar to the first exposure, it can be seen that the polarisation of the internal magnet realigned with the polarisation of the static magnetic field of the scanner. Orientations 90° and 270° also show a similar result. The first exposition provides a substantial demagnetisation of 85 and 77 percent, respectively. Again, the second exposure does not cause a significant change in magnetisation. In contrast to the other two orientations, the third exposure did not realign the internal magnets with the external magnetic field. Magnet strength remains low, decreasing slightly for 0° (79 percent) and increasing slightly for 180° (95 percent). Given that the demagnetisation around a 7.0T system can be quite severe (>100%), systems with this field strength are considered to be harmful for the functionality of the AIMD.

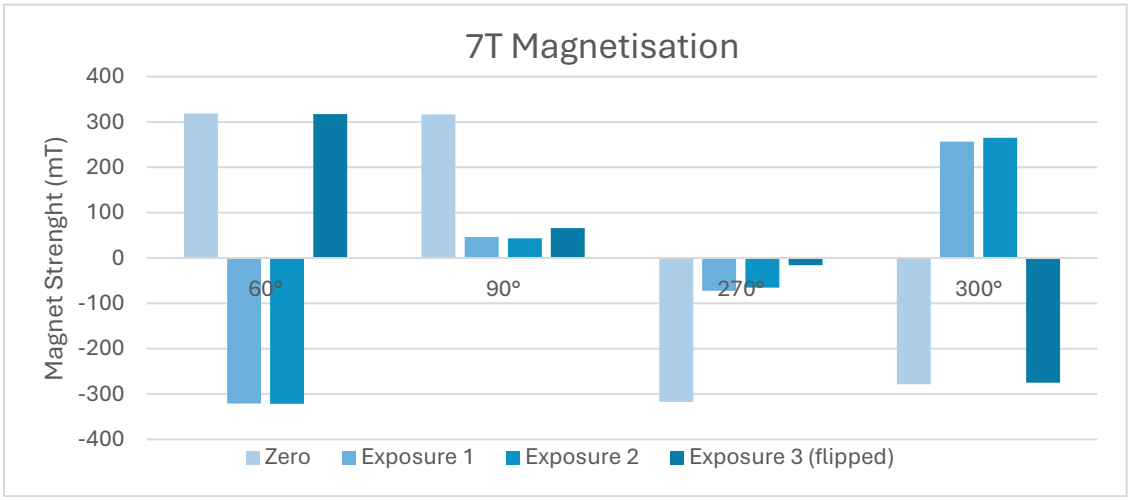

Figure 20 Magnetisation (mT) of the internal magnet after three exposures to the field of a Philips Achieva 7.0T system for baseplate angles 330, 0, 180 and 210 degrees.

4.2 Radio Frequency Field (B_1)

4.2.1 Simulation of RF heating

Figure 21 shows the spatial SAR distribution in a transverse cross-section of the ASTM phantom with the AIMD positioned longitudinally in the head of the phantom. The plot shows that heating is localized around both ends of the lead with the most significant heating found around the eighth, most distal, electrode. Energy absorption is quite localized with strong levels around the tissue-electrode interface and decreases rapidly with increasing distance from the electrode. Maximal point-SAR was found at the tissue-electrode interface and amounted to 2.38 W/kg. Note that the colour bar is logarithmic. This SAR corresponds to a temperature increase of roughly 0.2 degrees Celsius for an exposure period of 360 seconds, Eq. 2.7.

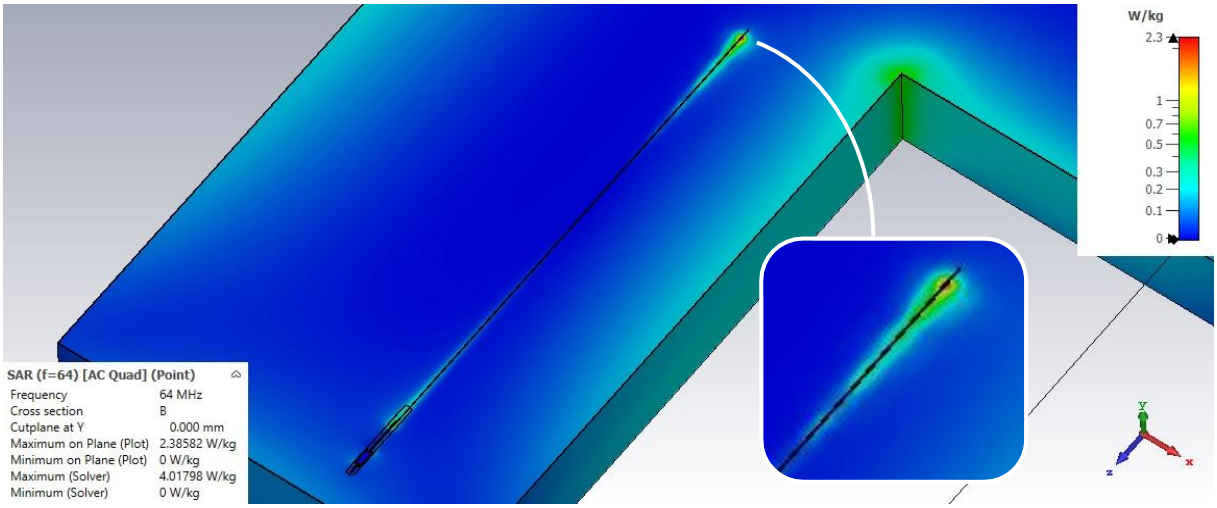

Figure 21 Transverse cross-section of the simulated point-SAR distribution for the AIMD positioned longitudinally in the head of the ASTM phantom. The phantom was placed with the AIMD in the isocentre.

Figure 22 depicts a similar situation with the AIMD positioned transversely in the torso of the ASTM phantom. Again, heating is found at both ends of the lead with the most significant heating around the eighth electrode. It is important to note that the degree of energy absorption, and thus the simulated SAR, is considerably lower than the situation in which the AIMD was positioned longitudinally in the head. In this case, maximal point-SAR at the tissue-electrode interface was found to amount to 0.55 W/kg. Again, note that the colour bar is logarithmic. The simulated SAR corresponds to an increase in temperature of roughly 0.05 degrees Celsius over 360 seconds.

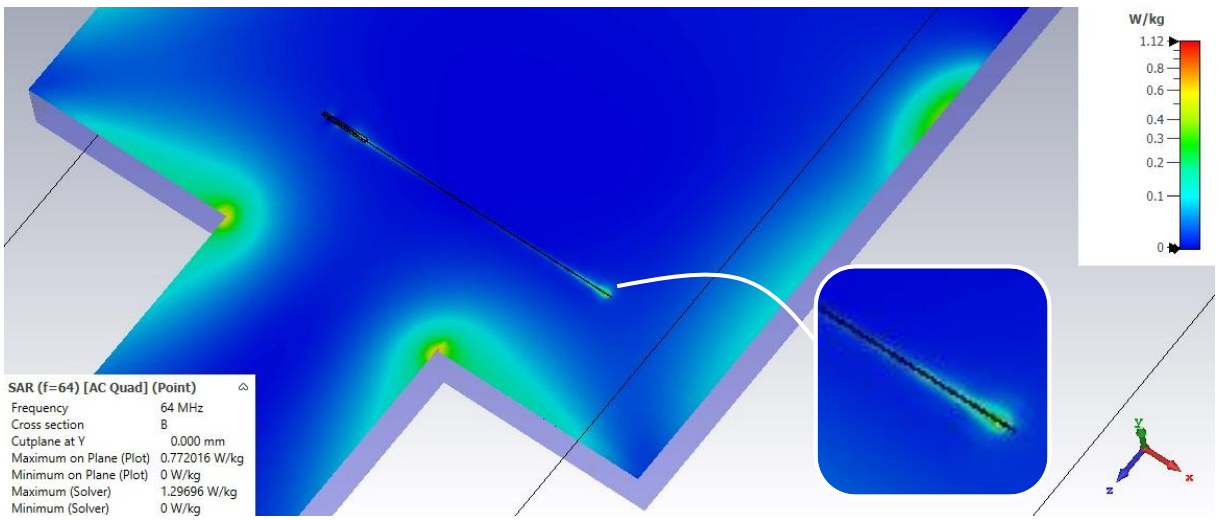

Figure 22 Transverse cross-section of the simulated point-SAR distribution for the AIMD positioned transversely in the torso of the ASTM phantom. The phantom was placed with the AIMD in the isocentre.

To get an idea of the dissipation of heat within the phantom, a 10 gram averaged SAR evaluation is shown in Figure 23. Because the heating is averaged over a larger volume, this provides an approximation of the effects of thermal conduction in tissue. The peak 10-g SAR around the eighth electrode is, smaller in comparison to surrounding values around the shoulder section of the phantom. This is partially because the heating is averaged over a greater volume.

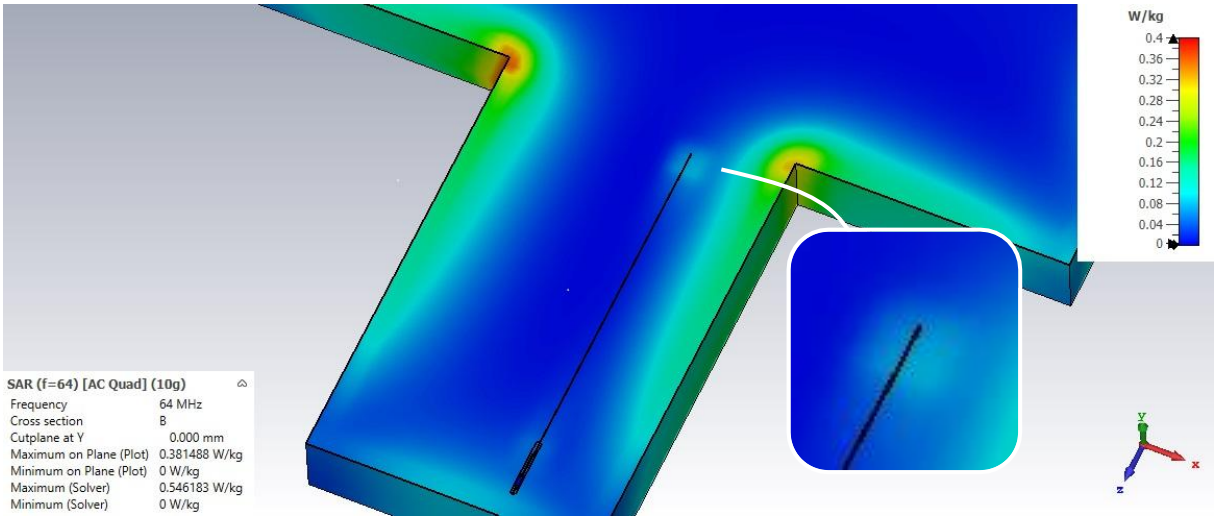

Figure 23 Transverse cross-section of the simulated 10-g SAR for the AIMD positioned longitudinally in the head of the ASTM phantom. The phantom was placed with the AIMD in the isocentre.

The results of the simulated RF heating (max. 2.3 W/kg) are within the safety limits set by the IEC 60601-2-33 (10 W/kg) and therefore, passed this test.

4.2.2 In-vitro validation RF heating

RF induced heating was validated in the ASTM phantom for a FSE sequence ran at maximum global SAR levels and for a scan duration of 6 minutes. Figure 24A illustrates RF induced heating (ΔT) around the eighth electrode of the AIMD with respect to a baseline measurement at the edge of the phantom. The AIMD was placed longitudinally in the head compartment, along the *z*-axis of the scanner. Heating shows a slight exponential pattern at the start of the measurement and transitions to a linear trend after roughly 150 seconds. Heating peaks at roughly 1.28 degrees Celsius after 360 seconds of exposure. The baseline increases slightly above zero degrees Celsius. In terms of the AIMD placed transversely in the torso of the phantom (Figure 24B), the heating is linear and significantly less in comparison to the longitudinal measurement peaking at 0.43 degrees Celsius.

The temperature profile of the measurements below was also used to determine the CEM43 for longitudinal and transverse AIMD using Eq. 2.8. This resulted in a CEM43 of 0.10 and 0.03, respectively.

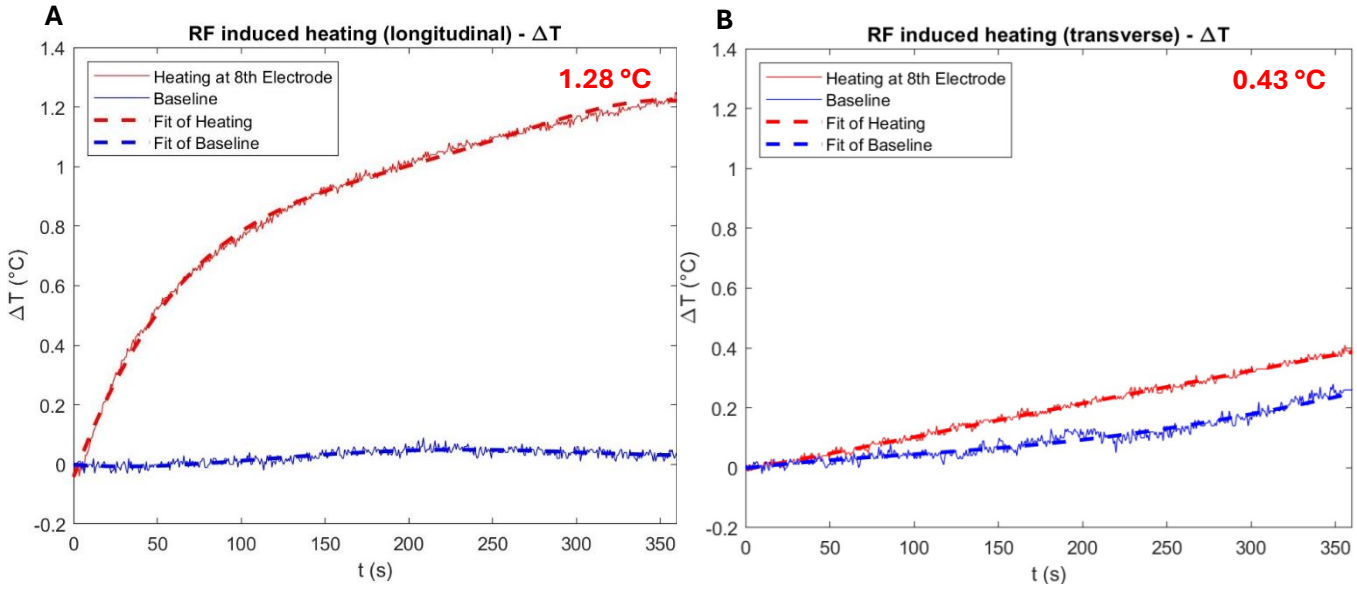

Figure 24 RF induced heating of the AIMD lead at the eighth electrode and baseline near the edge of the phantom. A) AIMD positioned longitudinally (along z) in the head. B) AIMD positioned transverse (along x) in the torso

In terms of the safety risks associated with RF induced heating, the results show that the worst-case (longitudinal) heating of 1.28 degrees Celsius exceeds the IEC 60601-2-33 limit of 0.85 degrees Celsius. However, the CEM43 values are significantly below the dose threshold of 21 implying that the risk of thermally induced tissue damage is small. Therefore, it is dependent on the safety limit you define. Since the ISO/TS 10974:2018 specifically defines the IEC 60601-2-33 limit, it is considered that the AIMD did not pass this test.

4.3 Gradient Field (G)

4.3.1 Validation of gradient field strength

The (dB/dt)-levels of the EPI sequence used for the gradient induced vibration and heating experiments are shown in Figures 25 and 26. Although the (dB/dt)-levels were determined for all axes of the scanner, the results along the *x*-axis are shown as these are most relevant for validating the requirements of the vibration and heating experiments. Figure 25 illustrates the difference between the strength of the gradients at the isocentre (A) and 30 centimetres from the isocentre (B). These positions can also be associated with a neuroimaging landmark (isocentre) or a cardiac landmark (Z+30cm). The ISO/TS 10974:2018 requires peak values greater than 63.7 T/s in the vibration experiment (section A.2.2, table A.2, [11]). Both positions meet this requirement. It is noticeable that although at the isocentre peak values of the gradients are higher, the RMS values increase as the distance from the isocentre increases. Although the values at the cardiac imaging landmark are closer to the requirement, both positions do not meet the requirement of 29.8 T/s (section 9.2.2., Table 5 [11]) set by ISO/TS 10974:2018 for RMS values for the heating experiment. Thus, Eq. 3.12 was used for temperature scaling.

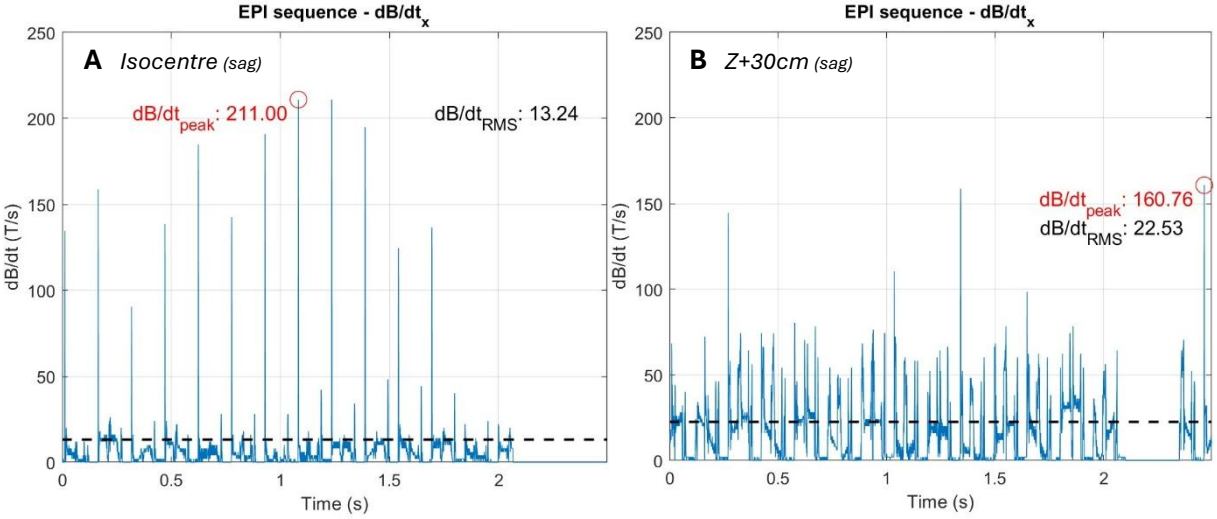

Figure 25 A) dB/dt-levels at the isocentre B) dB/dt-levels 30 centimetres from the isocentre

Figure 26 shows the effect of different imaging plane orientations on the strength of the measured gradients. Here it is important to mention that the search coil was oriented along the *x*-axis. It is noticeable that the transverse (A) and coronal (C) scan directions yield similar results. The sagittal scan direction (B) clearly provides the highest peak values. The RMS values differ minimally between all imaging plane orientations.

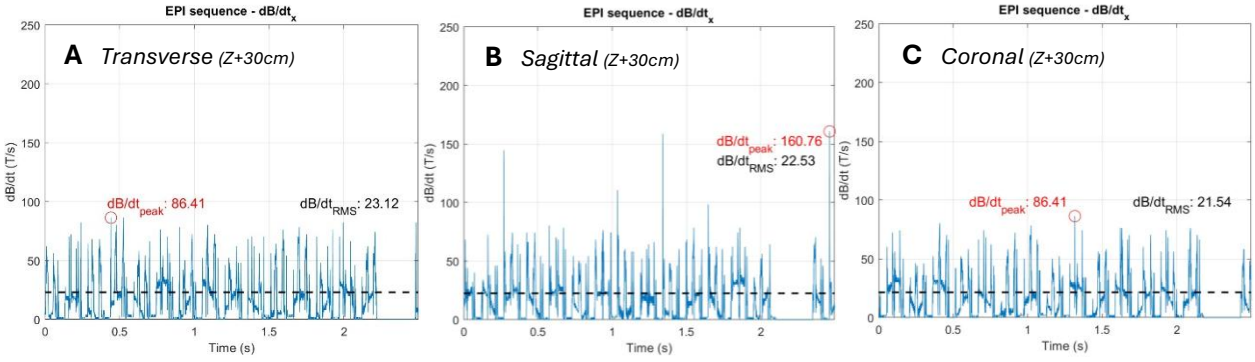

Figure 26 dB/dt-levels 30 centimetres from the isocentre for a A) Transverse B) sagittal and C) Coronal imaging planes

Table 12 shows that, in general, the (dB/dt)-values relative to the *x*-axis are the highest. Only for the peak values around the cardiac imaging landmark (Z+30cm), the $(dB/dt)_x$-values are not necessarily the largest. In this case, this is dependent on the imaging plane orientation. For a sagittal scan direction, the gradient along the *x*-axis is still the strongest. The results of the gradient strength validation were used to make considerations regarding the scan parameters of the gradient vibration and heating experiments.

Table 12 Overview of the gradient strength along all three axis for the isocentre and Z+30cm position. Gradient peak and RMS values are shown for each scan direction.

	$(dB/dt)_{RMS}$ (T/s)			$(dB/dt)_{peak}$ (T/s)		
	Transverse	***Sagittal***	***Coronal***	***Transverse***	***Sagittal***	***Coronal***
X_{ISO}	10.0	13.2	9.7	201.0	211.0	138.6
Y_{ISO}	4.4	4.6	4.1	38.2	42.2	30.1
Z_{ISO}	8.4	8.3	8.6	42.2	38.2	40.2
X_{Z+30cm}	21.5	22.5	23.1	86.4	160.8	86.4
Y_{Z+30cm}	9.4	9.1	9.5	98.5	70.3	110.5
Z_{Z+30cm}	8.1	9.0	8.8	88.4	104.5	118.6

The gradient waveforms that were measured by the search coil were also used to determine the duty cycle of the EPI sequence in MATLAB®. It was found that the gradients are active for approximately 62 percent of the time.

Sufficient $(dB/dt)_{peak}$-values were achieved exceeding the requirement of 63.7 T/s. The $(dB/dt)_{RMS}$-values were below the requirement of 29.8 T/s indicating the need for temperature scaling according to Eq. 3.12.

4.3.2 Gradient induced vibration

The AIMD was exposed to an EPI-sequence for a duration of 135 minutes. Functionality of the AIMD was tested using the external stimulator and electrodes impedances were verified through a Python-script. The external stimulator indicated successful calibration and stimulation. The Python script showed correct impedances between the electrodes. Considering magnet rattling, no audible magnet rattling was observed in any of the exposed AIMDs.

The device remained functional and therefore passed this test.

4.3.3 Gradient induced heating

Gradient induced heating was analysed in the ASTM phantom for the validated EPI sequence (3.3.1) and a scan duration of 30 minutes. Figure 27 illustrates gradient induced heating (ΔT) around the magnet of the AIMD with respect to a baseline measurement at the edge of the phantom. Interestingly, both the baseline and experimental temperatures decline indicating that there is no substantial heating around the magnet, rather suggesting that the background medium was cooling down. Given that the results of 4.3.1 indicated that the used EPI sequence did not comply with the $(dB/dt)_{RMS}$-requirement of the ISO/TS 10974:2018, temperature scaling is according to Eq. 3.12 [11] is required resulting in a scaling factor of 1.75, Eq. 4.1. However, since no gradient induced heating was observed, it is irrelevant to apply this scaling factor to the observed cooling, here.

$$\Delta T = \Delta T_{measured} \left[\frac{29.8}{22.53}\right]^2 = 1.75 \cdot \Delta T_{measured} \tag{4.1}$$

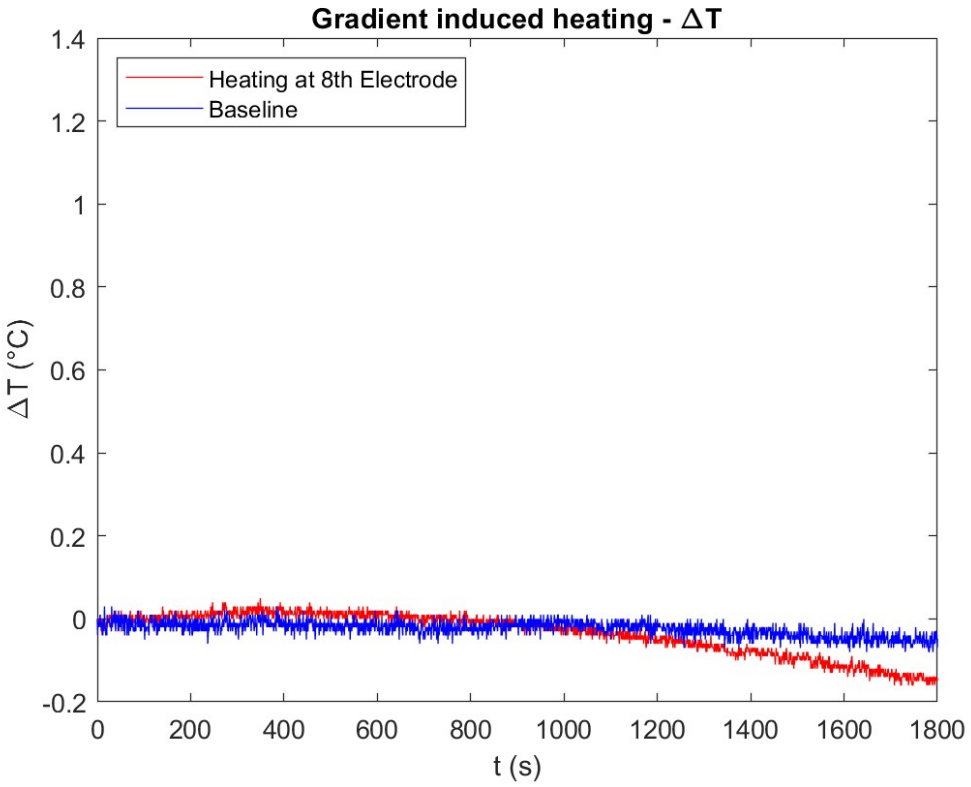

Figure 27 Gradient induced heating of the AIMD lead at the eighth electrode and baseline near the edge of the phantom.

Given that no significant heating has been observed after half an hour, gradient induced heating is well within the safety limits, therefore passing this test.

4.4 Combined fields test

The AIMD was exposed to nine clinical scan procedures. The test setup is shown in Figure 28. Table 13 indicates the clinical scan procedures that were run, the specific scan sequences that were executed and the result of the functionality test. Functionality of the AIMD was tested using the external stimulator. For all scan procedures, the external stimulator indicated successful calibration and stimulation. This proves that the AIMD remained functional and passed this test.

Table 13 Clinical scan procedures and specific scan sequences used during the Combined Fields Test along with AIMD status after exposure

Clinical Scan Procedure	Scan Sequence	AIMD Status
Brain	T2 FSE	Functional
Shoulder	T2 FSE	Functional
Cardiac	T1 TrueFISP	Functional
Breast	T2 FSE	Functional
Enterography	T1 TrueFISP	Functional
Liver	T1 FSE	Functional
Prostate	T2 FSE STIR	Functional
Knee	PD FSE	Functional
Thigh	T2 FSE STIR	Functional

Figure 28 Visualisation of the test setup of the Combined Fields Test. The ASTM phantom was placed on the patient table and the AIMD was located in the plastic container that was placed in the head compartment of the phantom

4.5 Image Artifacts

4.5.1 In-vitro quantification

Artifact sizes were determined with a MATLAB® script that masked all pixels that deviated more than 30 percent with respect to the reference image. Then, the dimensions of the artifact were measured from the centre of the slice to the border of the artifact as shown in Figure 29. The resultant artifact dimensions for the internal magnet and AIMD without magnet are shown in Table 12. Artifact dimensions were assessed along all three axis for a fast spin echo (FSE) and gradient echo (GRE) scan sequence. It is important to note that according to the standard, ASTM F2119 (section 7.3.1. [37]), the dimensions of the artifact are given as the radius of the artifact minus the radius of the AIMD. However, it was chosen to display the radii of the entire artifact in Table 12 since these dimensions are more relevant to indicate the loss of diagnostic value of the MR-image. Subtracting the AIMD radii (x = 11,5, y = 18.75 mm, z = 1.65 mm) would give a biased view of the actual size of the artifact.

It can be seen from Table 14 that, in each case, the dimensions of the GRE artifacts are larger than those of the FSE artifacts. The largest artifact (GRE) was obtained by orienting the magnet along the *y*-axis which resulted in a maximum radius of 128 mm. In the case of the AIMD without a magnet, the dimensions of the artifacts were consistently smaller. Again, the GRE artifacts were larger than the FSE artifacts. The largest (GRE) artifacts were obtained with the AIMD oriented along the *y*- and *z*-axes resulting in a maximum radius of 59 mm. The direction in which the artifact is the largest depends on the orientation of the object. Orientation along the *x*- and *y*-axes resulted in the largest radius along the *y*-axis of the image. In contrast, orientation along the *z*-axis resulted in the largest radius along the *x*-axis of the image.

Magnet Artifact (FSE - y)

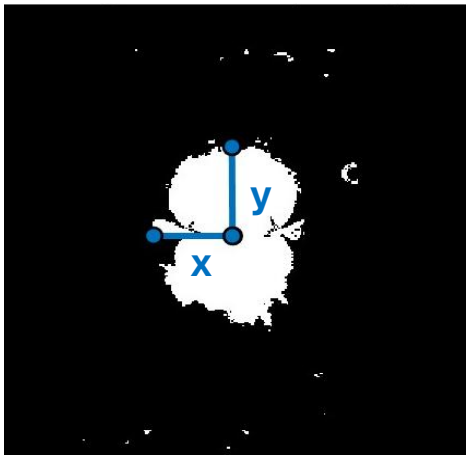

Figure 29 Sample visualisation of the determination process of the artifact size of the internal magnet oriented along the y-axis acquired with a FSE sequence.

Table 14 Artifact sizes of the internal magnet and AIMD along all three orientations for a FSE and GRE scan sequence

	Orientation	***Max. artifact radius FSE (mm) along X | Y***	***Max. artifact radius GRE (mm) along X | Y***
Magnet	*x*	74 | 90	94 | 121
	y	64 | 75	91 | 128
	z	93 | 77	107 | 100
AIMD *Without magnet*	*x*	21 | 35	30 | 47
	y	28 | 43	37 | 59
	z	29 | 34	34 | 59

Images have also been acquired with different readout directions. That is, both Right – Left (RL) and Head – Feet (HF). The readout direction does not significantly influence the magnitude of the artifact and the found radii correspond to the radii shown in Table 12. However, even though the artifacts do not increase in size, the readout direction can influence the shape of the artifact. This is shown in Figure 30AB and 30CD respectively. Figure 30AB illustrates that although both artifacts have similar sizes and magnitudes, the geometrical distortion is markedly different. Figure 30CD shows the shape- and orientational dependence of the artifact on readout direction which is indicated by the white arrow.

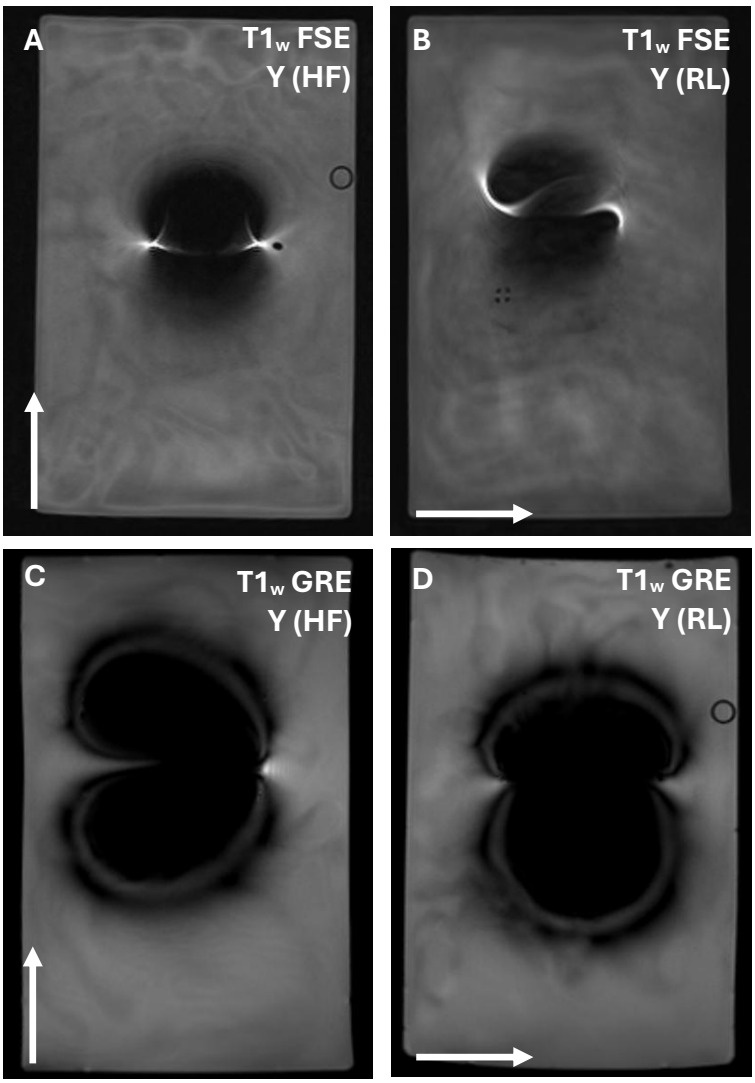

Figure 30 A) $T1_w$ FSE acquisition of the magnet oriented along Y with HF readout B) $T1_w$ FSE acquisition of the magnet oriented along Y with RL readout C) $T1_w$ GRE acquisition of the magnet oriented along Y with HF readout D) $T1_w$ GRE acquisition of the magnet oriented along Y with RL readout

4.5.2 In-vivo assessment

Image artifacts were also analysed in an in-vivo setting to determine the influence of the AIMD on the image to assess whether these complicate diagnostics in neuroimaging. Figure 31 shows two neuroimaging acquisitions with the internal magnet (AB) or for the AIMD without the magnet (CD). Images were acquired with a T2-weighted FSE sequence (AC) and a diffusion-weighted EPI sequence (BD). Most noticeable is the difference in the magnitude of the artifact which is dependent on the presence of the magnet. In Figure 31A, a clear signal void is present due to the magnet. This void disappears when the AIMD is scanned without an internal magnet, which is visible in Figure 31C. Here, no void is present but only a small distortion with hyperintensities around the AIMD. Diffusion weighted EPI images were created to induce the largest possible artifact which are evidently larger than the FSE artifacts. Again, the magnitude of the artifact is mainly determined by the magnet. Removal of the magnet resulted in a smaller artifact.

Although the magnitude of the artifact does not impose any safety hazards, the results indicate that having the AIMD implanted bilaterally will significantly reduce the diagnostic capabilities in the context of neuroimaging.

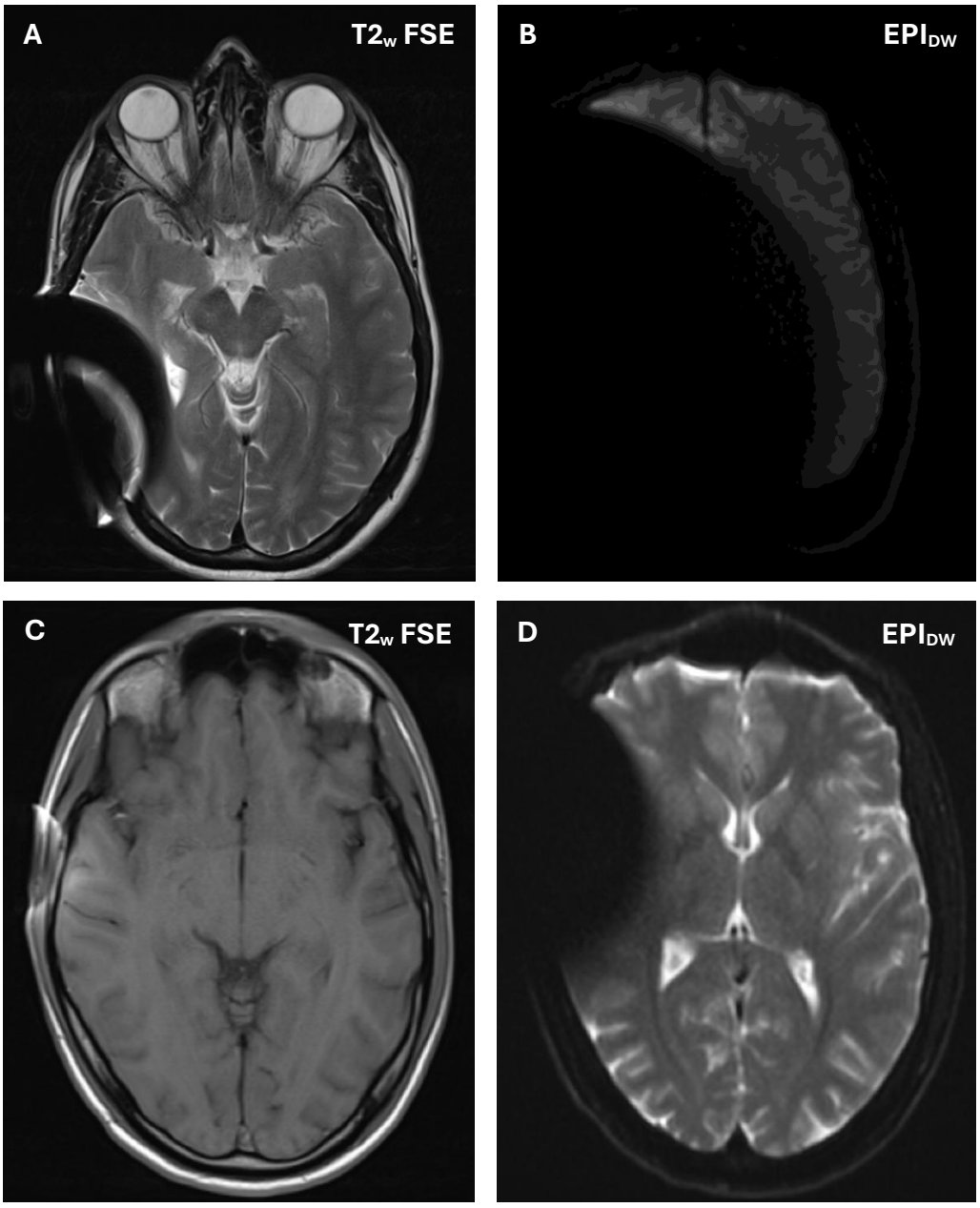

Figure 31 A) T2w FSE acquisition of the brain with the internal magnet B) DW EPI acquisition of the brain with the internal magnet C) T2w FSE acquisition of the brain with the AIMD without magnet D) DW EPI acquisition of the brain with the AIMD without magnet

5. Discussion

The aim of this research was to assess the MR compatibility of an innovative neurostimulation implant. The objective was to explore and identify potential safety hazards that arise from the interactions with the electromagnetic fields present in an MRI scanner. It is important to stress that while the discussion may state that a single interaction in itself does not pose a problem in terms of MRI safety or functionality, it is always necessary to consider the interplay of all interactions. A brief overview of the results in comparison to the established safety limits (section 2.4) is given in Table 15.

Table 15 Overview of the results per interaction mechanism in comparison to the safety limits

Hazard Mechanism	Safety limit	Result (1.5T)	
B_0 induced force	$F \leq 1.8$ N [1]	$F \leq 0.25$ N	✓
B_0 induced torque	$\tau \leq 0.043$ Nm [2]	$\tau > 0.068$ Nm	?
	$F \leq 5$ N [3]	$F \leq 4.47$ N [4]	?
B_0 induced demagnetisation	*To be determined*	Max 6%	?
RF induced heating	$\Delta T < 0.85$ °C OR	$\Delta T_{max} = 1.28$ °C	!
	CEM43 < 21	CEM43 = 0.10	✓
Gradient induced vibrations	Device remains functional	Functional	✓
Gradient induced heating	$\Delta T < 0.85$ °C OR	$\Delta T \approx 0$°C	✓
	CEM43 < 21	CEM43 = 0.11	✓
Combined Fields test	Device remains functional	Functional	✓

[1] *Comparison to the current generation of CIs [26]*
[2] *Maximal torque found for a current generation CI with a rotatable magnet [27]*
[3] *Comparison to older generations of CIs with an axial magnet [26]*
[4] *Maximal validated torque for the measured angles at isocentre (0°-200°). Angles beyond are likely to result in greater torques and thus, a greater resulting force.*

Translational force

The magnetically induced translational force on the AIMD at the bore entrance was found to be approximately 0.25 N in a 1.5T system, increasing to 0.49 N and 1.03 N for the 3.0T and 7.0T systems, respectively. Given the ultra-lightweight design of the AIMD, these forces exceed the gravitational acceptance criterion given in ASTM F2052 section 9.2 [28] over six times. Further interpretation by means of a comparative analysis with MR-compatible cochlear implants (CI) provided a better perspective on the risk related to these translational forces. This comparison is justified by the comparable design features and anatomical position shared between this AIMD and CIs. The comparison shows that the experimental translational forces acting on the AIMD are less than the maximal forces acting on the CIs found by Eerkens et. al. [26]. It is important to stress that this experimental assessment only considers the interactions with the static field while entering the bore along the centreline of the magnet. Although this represents the most probable configuration, there is a chance that the patient will move their head along the periphery of the bore where the spatial gradient is even higher. These conditions have not been included in this study. ASTM F2052 does not require a dedicated assessment of the translational forces near the edge of the bore. Hence, this was not included given the complexity of the measurement and the fact that a different test fixture was required. However, it is possible to estimate these forces based on the spatial field gradients in the documentation of the scanner (section 2.1). From this, we can estimate that the peripheral translational forces are expected to be below the maximal values found by Eerkens et. al. and can therefore also be considered safe.

Torque

The magnetically induced rotational force (torque) on the AIMD is strongly dependent on the orientation of the internal magnet with respect to the external magnetic field. Although a patient will typically be in the scanner in only a limited number of orientations, all possible orientations should be considered when evaluating safety. It is important to mention that the results obtained with this test setup did not comply with ASTM F2213 section 7.5.1.5 [30] because deflections greater than 25 degrees were observed. For a baseplate rotation beyond 200 degrees, this deflection exceeded 90 degrees, and further measurements became highly inaccurate. This problem could have been solved by using a stiffer torsional spring in the setup. However, obtaining an MR safe torsional spring with a higher spring constant and maximal deflection of 25 degrees can be rather difficult, as also described by Stoianovici et. al [29]. The nylon wire used in our configuration also showed slight elastic deformation during the measurements, but since this deformation was mostly elastic, no impact on the accuracy of the results is expected. Although, due to this shortcoming, the test fixture did not strictly meet the requirement of the standard, the values obtained still give a reasonable indication of the torque on the AIMD. This is because the deflections observed in the 1.5T system were validated with a force meter outside the scanner which calibrated the test setup and made the obtained results more reliable. Although this validation is thought to be the closest approximation of the actual torque, this method also introduced an error due to the fact that the platform is pulled at a slight angle and the force is only applied at one point. These effects have been minimized through the use of bearings in the setup and through a correction in the mathematical approximation of the torque. Part of the validation curve was extrapolated based on the linear course at the beginning of the curve where the angle under which the platform is pulled, and thus the error, is the smallest. The exact magnitude of the error is unknown but estimated to amount to roughly 5 percent, up to a deflection angle of 60 degrees.

The gravitational torque (ASTM F2213 section 4.4 [30]) is exceeded by a factor of ±75. Consequently, the magnetically induced torque is also compared to the values of CIs with MR compatibility labelling established by Eerkens et. al. [26]. Validation of the torque resulted in a maximal torque of 0.068 Nm, which corresponds to a force of 4.47 N acting on the edge of the stimulator unit. It is expected that, with a proper test fixture, even higher torques could have been measured given the theoretical approximation of 0.16 Nm and the course of the graph at knee location (0°-360°) where the torque still increased significantly for baseplate rotation beyond 200 degrees. The experimentally determined torque exceeded the torque found for the system with the rotatable magnet (0.043 Nm) [27]. This does not necessarily imply that the AIMD is not safe, but rather gives an idea of the torque with which other devices obtained MRI compatibility labelling. The force acting on the stimulator unit is just below the force induced on CIs with an axial magnet. Newer models of CIs incorporate a diametric or fully rotating magnet resulting in a force as low as 3 Newton [26]. The minimal torque of rotatable magnets was verified internally using our test fixture. This resulted in a deflection of zero degrees. The observed torque is thought to arise from the inertia of magnet alignment and is thus not constant. Although the AIMD of this research shows a torque that is comparable to some of the earlier generations of CIs, the innovation of rotating magnets has resulted in exceptionally low torques in the newer generations of devices. The need for low torque magnets is addressed in the article by Young et. al. [38] in which they found that for CIs with an axial magnet similar to the one used in our study, a magnet-related complication occurred in approximately 33 percent of cases (n=13). This refers to, either rotation or dislocation of the internal magnet [38]. Rupp et. al. [39] found magnet-related complications in 50 out of 251 cases (21.6%) of which 27 magnet dislocations (11.7%). No

dislocations were observed for CIs with rotatable magnets. Given that torque scales with the field strength of the scanner and the fact that for the 3.0T and 7.0T systems, measurements were only made for the zero orientation, it is anticipated that the torque on the AIMD in 3.0T and 7.0T systems is also not safe. With regards to the 1.5T system, a proper bandage protocol can reduce, but not eliminate, the risk of rotation and dislocation of the magnet or AIMD [26]. Interestingly, some experts recommend removing the internal magnet while others recommend not removing it. Removing the magnet results in two surgical procedures, regardless. Not removing the magnet with a potential magnet-related complication, results in (1) no surgery in case of no complication or (2) only one revision surgery in case of a complication [26]. Not to mention the potential discomfort for the patient. Ultimately, to achieve MR compatibility labelling, the requirements of regulatory authorities such as the FDA and EMEA are critical. The specific torque requirements of these institutions are unknown, making it difficult to give an unequivocal conclusion regarding the safety of rotational forces in a 1.5T system. Thus, a definitive conclusion on the safety of this AIMD in a 1.5T environment can only be established once the requirements of regulatory authorities are available and, most importantly, a full assessment, including the angles beyond 200 degrees with a test fixture that complies to ASTM F2213, has been done.

Demagnetisation

Demagnetisation was tested for the orientations a patient could logically adapt by moving their head in the scanner. Demagnetisation of a few percent was found for the 1.5T system, which can be partially attributed to the accuracy of the Gauss meter and variability in the measurement protocol. The observed demagnetisation is unlikely to harm the quality of the transcutaneous coupling of the AIMD and the external stimulator. Remarkably, during the exposures to the 1.5T static magnetic field, the magnet with orientation 300 degrees initially demagnetised quite substantially (±20%). The experiment was repeated for this orientation in which this substantial demagnetisation was no longer observed. Therefore, the initial anomalous result was not included. It is not clear why the first magnet did demagnetise significantly after exposure to the 1.5T field. It is possible that this was due to a defective magnet. However, this does show that, although the general trend is that no significant demagnetisation at 1.5T, there may be exceptions in which the magnet demagnetises even at this field strength.

For the 3.0T and 7.0T systems, significant orientational-dependent demagnetisation was clearly observed. In the 3.0T system, the least demagnetisation was found for orientations that were roughly orthogonal (80° 270°) to the direction of the external magnetic field. Deviating further from these orientations increased the degree of demagnetisation. The orientational dependence may be explained using magnetic anisotropy (section 2.1) which implies that a cylindrical magnet (partially) aligned with the *z*-axis of the field (60° 120°) will be harder to (de)magnetise (higher N) whereas a cylindrical magnet orthogonal to the external magnetic field (90°) is easier (de)magnetised (lower N). This theory does not correspond to the results of the demagnetisation experiment where the exact opposite seems to take place. Magnets with a smaller demagnetizing factor (N) are less susceptible to demagnetisation while magnets with a larger demagnetizing factor are demagnetised more severely. This may be explained by the reverse nature of demagnetisation which may cause an opposite effect to magnetisation theory. That is, a smaller N could indicate a weaker demagnetizing field that does not assist the demagnetisation induced by the external magnetic field causing the magnet to better retain its magnetisation. In contrast, a larger N could imply a stronger demagnetizing field that assists the external field making it more susceptible to demagnetisation [18] [40]. In essence, the demagnetizing field is expected to resist the external magnetic field during magnetisation and assist the external magnetic field during demagnetisation. However, there is little literature describing the physical principle of

demagnetisation and the role of demagnetisation factors to support this hypothesis. Although the underlying process of demagnetisation is not completely understood, the main conclusion is that 3.0T and 7.0T MRI systems can lead to significant demagnetisation of the internal magnet making any interaction with such systems an undesirable risk to the functionality of the AIMD.

Majdani et. al. [21] and Dubrulle et. al. [22] considered the demagnetisation of Cochlear Implants in 3.0T systems. Although it is difficult to compare the results because different types of magnets with different susceptibility to demagnetisation were used, it is possible to examine general trends in the demagnetisation process. Similar to our results, a clear orientational dependence is visible in both papers. However, both Madjani et. al. and Dubrulle et. al. see little demagnetisation up to roughly 85 degrees where the demagnetisation of this research was found to be substantial, even for the smaller angles. In line with our results, the demagnetisation in both articles increases strongly as the angle increases beyond 90 degrees. These differences may be due to the type of magnet within the device and its susceptibility to demagnetisation.

Heating

A conservative approach was used in the analysis of RF-induced heating. We chose to simulate the RF heating in an aqueous medium, having a permittivity (78) that is considerably higher than tissue (bone: 16.7, fat: 13.6). These properties result in a shorter resonant length of the device which will increase coupling between the RF field and the lead and cause increased levels of RF heating. As an insufficient amount of HEC was available at the time of the experiment, only a part of the phantom was filled with HEC and the rest was supplemented with saline. This may have affected the distribution of RF within the phantom. However, since the heating occurred fairly localised around the AIMD, it is expected that the HEC-filled plastic container formed a sufficient barrier around the AIMD that minimised the effect of the saline. In future research, it is desirable to perform the experiment with a phantom completely filled with HEC to avoid introducing inaccuracies in the RF loading and thermal properties. The experimental results showed significant RF-induced heating whose magnitude was strongly dependent on the orientation of the AIMD, similar to our simulation results and literature [41]. Longitudinal placement in the head compartment caused heating of 1.28 degrees Celsius exceeding the safety limit of 0.85 degrees Celsius. However, given the length of the lead, it is impossible for the lead to be positioned in this orientation in an anatomically correct situation. In a normal situation, the lead partially moves up the side of the head (along the *y*-axis) after which it deflects over the forehead (along the *x*-axis). This automatically will reduce the RF coupling with the background RF transmit field. This orientational dependence was confirmed by transverse (along *x*) placement of the lead in the torso compartment. This produced a heating of 0.48 degrees Celsius which is within the safety limit. Moreover, in a clinical situation, there will be active cooling mechanisms such as perfusion and airflow that will further reduce the degree of heating [13][23]. Although the ISO/TS 10974:2018 clearly refers to the SAR limit given in IEC 60601-2-33, this is not a strict requirement as long as it can be demonstrated that the level of heating will not be harmful to the patient. Manufacturers often use the CEM43 to indicate the implications of heating in terms of biological effects and potential tissue damage. The CEM43-analysis showed that it is highly unlikely that the thermal dose would cause any tissue damage. To provide an unequivocal conclusion regarding the safety of RF induced heating, additional research is essential in which the actual conditions (lead trajectory, heterogenous phantom, cooling mechanisms) are more accurately approximated rendering the conservative safety margins that have been taken into account in this analysis redundant. It is likely that a more accurate configuration would result in a temperature increase that is within the safety limit established in the ISO/TS 10974:2018, dismissing the need for elaboration. Although this research tried to maximise RF heating by maximising the antenna

effect using a High Permittivity Medium (HPM) to optimise the resonance length of the AIMD and enhance field coupling, experts recommended that future research should also consider RF heating in a Low Permittivity Medium (LPM) characterized by a lower permittivity and conductivity. They suggest this could alter the distribution of RF power deposition and even increase the antenna effect as the high conductivity of a HPM could have damped the antenna effect. Introducing a LPM may reduce damping due to the lower conductivity which could lead to more significant heating around the AIMD. This reasoning is supported by Yeung et. al [42] who have shown that a medium with lower conductivity can lead to more significant heating and a higher safety risk. However, future research will have to reveal whether this also holds for this AIMD. Gradient induced heating was not observed in our experiments. This is most likely due to the fact that this degree of heating (theoretical: 0.15 °C) is minimal and induced over a considerable period of time, half an hour, allowing sufficient time for the heat to be dissipated by conduction.

Functionality

Another important aspect is maintaining the functionality of the AIMD after exposure to the EM fields of an MRI scanner. Dysfunctionality of the AIMD does not directly pose any safety concerns given that unintended stimulation or failure of stimulation does not have direct life-threatening implications for the patient. However, it may result in the need for re-implantation of a new device which is obviously not desirable. The functionality experiments were performed at 1.5T and covered the lifetime MRI exposure of 99.2 percent of the population. More extensive testing could cover 99.9- or 99.99 percent of the population but more prolonged exposure of the AIMD to the EM fields of the scanner is not expected to lead to malfunctioning since the current, quite substantial, exposure did not reveal any indications of malfunctioning. In terms of functionality, it is arguable that the AIMD retains its functionality around 1.5T MRI systems. Exposure to 3.0T and 7.0T static magnetic fields did not cause malfunctioning of the device. However, even though no further functionality tests were conducted for 3.0T and 7.0T systems, based on the prior observed demagnetisation it can be stated that functionality is jeopardised in general around these systems.

Image Artifacts

In terms of image artifacts, it is important to note that this has no impact on the safety of the AIMD. Also, this is only relevant for acquisitions of the head. The results have shown that the internal magnet of the implant causes substantial spherical voids and distortions in the MR images ($r_{max} = 128$ mm). Understandably, once the AIMD is implanted bilaterally, this results in two substantial artifacts, voiding a large part of the anatomy. This is confirmed by the in-vivo analysis. Here, voids and distortions that impact a large part of the brain are evident. Although their magnitude is sequence dependent, all sequences strongly influence the diagnostic capabilities and it is expected that suspicion of, for example, a brain tumour will lead to surgical removal of the AIMD to obtain valuable images of the anatomy. In contrast, analysis of the AIMD without internal magnet revealed substantially smaller artifacts ($r_{max} = 59$ mm). In the in-vivo acquisitions a large void does not necessarily appear if no magnet is present. While minor distortions and shadows are present in the FSE acquisition, the majority of images remain clear of artifacts, preserving diagnostic image quality within the brain. It was not possible to reduce the magnitude of the artifact by changing sequence parameters such as the readout direction.

Lastly, it is important to mention that this research does not provide a full analysis of MR compatibility as specified in ISO/TS 10974:2018. As mentioned in the introduction, the clauses concerning unintended stimulation (13) and RF (15) and Gradient (16) malfunction were not examined. Future research will have to establish the MR compatibility of these aspects.

6. Outlook

When considering MR conditionality, it is important to evaluate two aspects. First, the MR safety of the current version of the AIMD and second, the design modifications that could be made in future versions of the implant to increase the safety of the AIMD or achieve MR conditionality. In the light of Table 15, it can be argued that the current version of the AIMD is close to MR conditionality. The current analysis of RF induced heating exceeds the safety limit but it is expected that a more accurate approach could meet the safety limit. The other aspects fall within the specified safety limits. However, in terms of torque, it can be argued that the axial magnet imposes an excessive risk of complications considering the articles by Young et. al. [38] and Rupp et. al. [39]. This risk can be partially mitigated by introducing a bandage protocol but in an optimal case, implementing an innovative internal magnet in the design will ensure a safer torque.

Future generations of the AIMD should account for the rotational force (torque) and potential demagnetisation around systems with higher field strengths (3.0T - 7.0T). To achieve MRI compatibility in 1.5T systems, torque may be an obstacle due to the risk of magnet related complications. It may be feasible to make modifications to the design of the AIMD to reduce these hazards. The magnetically induced torque can be reduced by implementing an internal magnet with smaller dimensions or a lower magnetic dipole moment. This will reduce the attraction by the static magnetic field of the MRI system given that torque scales with the magnetic dipole moment of the magnet which depends on its volume and remanence, Eq. 2.1 and 2.3. A reduction in the strength of the internal magnet may be problematic for the performance of transcutaneous coupling with the external stimulator and may require a stronger external magnet. Also, a weaker magnet is more susceptible to demagnetisation potentially leading to demagnetisation around 1.5T systems. This is not the case for a magnet with smaller dimensions but the same remanence (B_r). The risks related to torque can also be reduced by increasing the dimensions of the stimulator unit of the AIMD which will distribute the induced forces over a larger area and thus reduce their magnitude and the probability of rotation or dislocation of the AIMD. This would require a larger incision for placement of the device which is not desirable.

In the world of Cochlear Implants, the implementation of a rotatable magnet is a common solution to eliminate excessive rotational force without major drawbacks. This technique was developed because dislocation of the magnet would require surgical intervention with the risk of infection and explantation of the device [39]. There are two types of rotatable magnets (1) diametric rotatable magnets and (2) three dimensional rotatable magnets. These are shown in Figure 32 along with a visualisation of the current axial magnet. It is evident that where the axial magnet may dislodge from its housing or start to exert forces on the AIMD, the rotating magnets can rotate and align with the external magnetic field, resulting in a significant reduction in torque.

Additionally, a rotatable magnet can potentially reduce demagnetization of the internal magnet at higher field strengths (3.0T – 7.0T) because the internal magnet is able to align with the static magnetic field, eliminating the orientational dependence between the two. However, this is an assumption and there is no supportive literature on this matter.

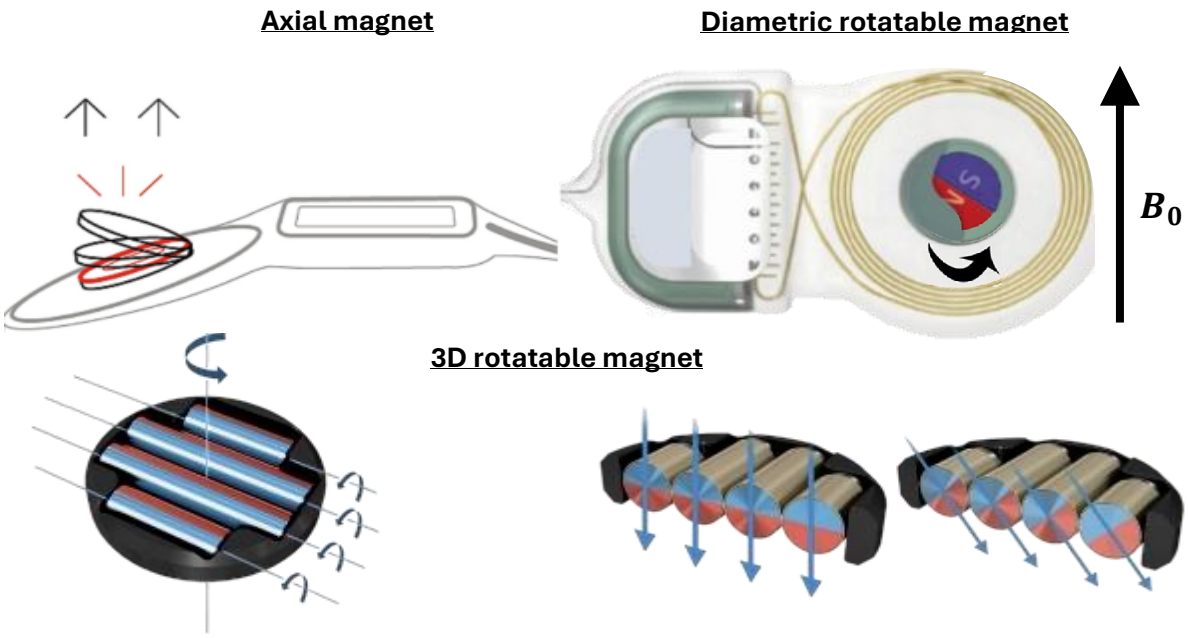

Figure 32 Visualisation of the translational and rotational forces on axial, diametric rotatable and three dimensional rotatable magnets when exposed to an external magnetic field [43][44]

Although the current RF-induced heating analysis exceeded the safety limit, it is too early to classify the AIMD MR-unsafe. As mentioned in the discussion, a more accurate analysis is required in which in the RF coupling is approached in a more anatomically realistic configuration. Should this analysis also indicate that the RF heating exceeds the safety limit, there are still a number of options that could be considered to achieve MR compatibility regardless. That is, either modifications to the design of the AIMD or restrictions on the acquisition protocols of the MRI scanner. The following possible modifications to the design are suggested in literature [23]:

(1) Increasing the resistivity of the lead
(2) Increasing the capacitance of the lead insulation to attenuate RF wave propagation
(3) Implementing RF chokes or traps that block RF currents at the Larmor frequency
(4) Implementing inductances or capacitances along the lead
(5) Implementing RF shielding along the lead

Given the ultra-thin design of the AIMD in this research, some of these options will be difficult or even not feasible. The options might also interfere with the functionality of the lead. Therefore, it is easier for the manufacturer of the AIMD to establish RF transmission restrictions in the MRI manual prescribing SAR restrictions that reduce RF power deposition and result in reduced heating around the implant [23].

7. Conclusion

In consideration of the results a conclusion can be drawn regarding the safety of the neurostimulation AIMD within a MRI environment. The static magnetic field appears to be the main problem when a patient with the AIMD would undergo an MRI scan. Although the translational force and demagnetisation, at least in a 1.5T system, do not seem to pose a problem, the rotational force (torque) does create a potential safety hazard. The torque creates substantial forces on the AIMD, resulting in potential rotation and dislocation of the device. This risk can potentially be mitigated with a proper bandage protocol, but given the innovations in the world of Cochlear Implants and the lack of knowledge of the specific safety limits, it is unclear whether the torque complies with modern safety requirements. No gradient induced heating was observed. In contrast, RF induced heating in a conservative configuration has shown safety limits may potentially be exceeded. Further research is required to analyse whether a more anatomically accurate situation would comply with safety regulations or to justify assessment in terms of CEM43. Functionality of the AIMD does not seem to be a problem in a 1.5T system. Experiments have shown that the AIMD remains functional after prolonged and intensive scanning procedures. Also, no significant demagnetisation occurred. Although functionality has not been analysed comprehensively for the 3.0T and 7.0T systems, it is clear that these field strengths can lead to complete demagnetisation of the magnet which is harmful to the functionality of the transcutaneous coupling and thus, the AIMD in general. Finally, although image artifacts do not pose a safety risk, the AIMD has been shown to cause substantial image artifacts rendering neuroimaging with the AIMD infeasible at clinical field strengths. The AIMD will have to be removed when clinical examination with MRI is required. Overall, it can be concluded that the AIMD approaches MR compatibility labelling on most aspects of the ISO/TS 10974:2018 but in terms of torque and RF heating, fundamental challenges still need to be overcome.

References

[1] Kung D, Rodriguez G, Evans R. Chronic Migraine: Diagnosis and Management. Neurol Clin. 2023 Feb;41(1):141-159. doi: 10.1016/j.ncl.2022.05.005.

[2] Stovner LJ, Andree C. Prevalence of headache in Europe: a review for the Eurolight project. J Headache Pain. 2010 Aug;11(4):289-99. doi: 10.1007/s10194-010-0217-0.

[3] Hovaguimian A, Roth J. Management of chronic migraine. BMJ. 2022 Oct 10;379:e067670. doi: 10.1136/bmj-2021-067670.

[4] Kok L, Koopmans C. Economische effecten van migraine. Amsterdam: SEO Economisch Onderzoek; 2021. 2021-42 [Online]. Available at: https://www.seo.nl/publicaties/economische-effecten-van-migraine/

[5] Han X, Yu S. Non-Pharmacological Treatment for Chronic Migraine. Curr Pain Headache Rep. 2023 Nov;27(11):663-672. doi: 10.1007/s11916-023-01162-x.

[6] Ashkan K, Sokratous G, Göbel H, Mehta V, Gendolla A, Dowson A, Wodehouse T, Heinze A, Gaul C. Peripheral nerve stimulation registry for intractable migraine headache (RELIEF): a real-life perspective on the utility of occipital nerve stimulation for chronic migraine. Acta Neurochir (Wien). 2020 Dec;162(12):3201-3211. doi: 10.1007/s00701-020-04372-z.

[7] Northern Pain Centre. Occipital nerve stimulation [Internet]. St. Leonards (AU): Northern Pain Centre; [cited 2025 Jun 19]. Available from: https://www.northernpaincentre.com.au/interventional-treatments-innovations/spinal-cord/occipital-nerve-stimulation/

[8] Fierens G, Standaert N, Peeters R, Glorieux C, Verhaert N. Safety of active auditory implants in magnetic resonance imaging. J Otol. 2021 Jul;16(3):185-198. doi: 10.1016/j.joto.2020.12.005.

[9] Erhardt JB, Fuhrer E, Gruschke OG, Leupold J, Wapler MC, Hennig J, Stieglitz T, Korvink JG. Should patients with brain implants undergo MRI? J Neural Eng. 2018 Aug;15(4):041002. doi: 10.1088/1741-2552/aab4e4.

[10] Al-Dayeh L, Rahman M, Venook R. Practical Aspects of MR Imaging Safety Test Methods for MR Conditional Active Implantable Medical Devices. Magn Reson Imaging Clin N Am. 2020 Nov;28(4):559-571. doi: 10.1016/j.mric.2020.07.008.

[11] International Organization for Standardization (ISO), “Assessment of the safety of magnetic resonance imaging for patients with an active implantable medical device,” ISO, Geneva, Switzerland, Tech. Specification 10974, 2018. [Online]. Available at: https://www.iso.org/standard/65055.html

[12] McRobbie DW, Moore EA, Graves MJ, Prince MR. MRI from Picture to Proton. 2nd ed. Cambridge: Cambridge University Press; 2006.

[13] Panych LP, Madore B. The physics of MRI safety. J Magn Reson Imaging. 2018 Jan;47(1):28-43. doi: 10.1002/jmri.25761.

[14] SM Magnetics. Sintered NdFeB – Neodymium Iron Boron. Pelham (AL): SM Magnetics; [Cited May 15 2025]. Available at: https://smmagnetics.com/pages/neodymium-ndfeb

[15] Philips Healthcare. Philips Achieva 3.0T TX: Technical Description. Release 5. Amsterdam: Philips Healthcare.

[16] Jackson DP. Dancing paperclips and the geometric influence on magnetization: A surprising result. American Journal of Physics. American Association of Physics Teachers (AAPT); 2006 Apr. 1;74(4):272–279.

[17] Panych LP, Kimbrell VK, Mukundan S Jr, Madore B. Relative Magnetic Force Measures and Their Potential Role in MRI Safety Practice. J Magn Reson Imaging. 2020 Apr;51(4):1260-1271. doi: 10.1002/jmri.26924. Epub 2019 Sep 11.

[18] Chikazumi S. Physics of ferromagnetism. 2nd ed. Oxford: Oxford University Press; 2009.

[19] Wysin GM. Demagnetization fields. 2012 [Cited Oct 20 2025]. p. 1–16. Available from: https://www.phys.ksu.edu/personal/wysin/notes/demag.pdf

[20] Prozorov R, Kogan VG. Effective Demagnetizing Factors of Diamagnetic Samples of Various Shapes. Physical Review Applied. American Physical Society (APS); 2018 Jul. 27;10(1).

[21] Majdani O, Leinung M, Rau T, Akbarian A, Zimmerling M, Lenarz M, Lenarz T, Labadie R. Demagnetisation of cochlear implants and temperature changes in 3.0T MRI environment. Otolaryngol Head Neck Surg. 2008 Dec;139(6):833-9. doi: 10.1016/j.otohns.2008.07.026.

[22] Dubrulle F, Sufana Iancu A, Vincent C, Tourrel G, Ernst O. Cochlear implant with a non-removable magnet: preliminary research at 3-T MRI. Eur Radiol. 2013 Jun;23(6):1510-8. doi: 10.1007/s00330-012-2760-3.

[23] Winter L, Seifert F, Zilberti L, Murbach M, Ittermann B. MRI-Related Heating of Implants and Devices: A Review. J Magn Reson Imaging. 2021 Jun;53(6):1646-1665. doi: 10.1002/jmri.27194.

[24] International Electrotechnical Commission (IEC). IEC 60601-2-33:2010+AMD1:2013+AMD2:2015 CSV: Medical electrical equipment – Part 2-33: Particular requirements for the basic safety and essential performance of magnetic resonance equipment for medical diagnosis. Geneva: IEC; 2015.

[25] International Organization for Standardization. Implants for surgery—Active implantable medical devices—Part 3: Implantable neurostimulators (ISO 14708-3:2022) [Internet]. Geneva: ISO; 2022 [cited 2025 Jun 19]. Available from: https://www.iso.org/standard/60539.html

[26] Eerkens HJ, Smits C, Hofman MBM. Cochlear Implant Magnet Dislocation: Simulations and Measurements of Force and Torque at 1.5T Magnetic Resonance Imaging. Ear Hear. 2021 Sep/Oct;42(5):1276-1283. doi: 10.1097/AUD.0000000000001013.

[27] Tysome JR, Tam YC, Patterson I, Graves MJ, Gazibegovic D. Assessment of a Novel 3T MRI Compatible Cochlear Implant Magnet: Torque, Forces, Demagnetization, and Imaging. Otol Neurotol. 2019 Dec;40(10):e966-e974. doi: 10.1097/MAO.0000000000002407.

[28] Standard Test Method for Measurement of Magnetically Induced Displacement Force on Medical Devices in the Magnetic Resonance Environment: 100 Barr Harbor Drive, Standard F2052-21, ASTM International, West Conshohocken, PA, USA, 2022. [Online]. Available at: https://www.astm.org/f2052-21.html

[29] Stoianovici D, Sharma K, Cleary K. Measurement of Magnetically Induced Torque on Lightweight Medical Devices in the Magnetic Resonance Environment for ASTM F2213. IEEE Trans Biomed Eng. 2024 Jan;71(1):36-44. doi: 10.1109/TBME.2023.3291179.

[30] Standard Test Method for Measurement of Magnetically Induced Torque on Medical Devices in the Magnetic Resonance Environment: 100 Barr Harbor Drive, Standard F2213-17, ASTM International, West Conshohocken, PA, USA, 2017. [Online]. Available at: https://www.astm.org/f2213-17.html

[31] Budynas, Richard G., and Ali M. Sadegh. 2020. *Roark's Formulas for Stress and Strain*. 9th ed. New York: McGraw-Hill Education.

[32] Beer FP, Johnston ER Jr, DeWolf JT, Mazurek DF. Mechanics of materials. 7th ed. New York: McGraw-Hill Education; 2015.

[33] Overview of materials for Nylon 66/6. MatWeb – The Online Materials Information Resource. Matweb.com. 2025. Accessed June 19, 2025. Available from: https://www.matweb.com/search/datasheet_print.aspx?matguid=26386631ec1b49eeba62c80a49730dc4

[34] Standard Test Method for Measurement of Radio Frequency Induced Heating On or Near Passive Implants During Magnetic Resonance Imaging: 100 Barr Harbor Drive, Standard F2182-19e2, ASTM International, West Conshohocken, PA, USA, 2020. [Online]. Available at: https://www.astm.org/f2182-19e02.html

[35] Muslov SA, Polyakov DI, Lotkov AI, Stepanov AG, Arutyunov SD. Measurement and Calculation of Mechanical Properties of Silicone Rubber. Russian Physics Journal. Springer Science and Business Media LLC; 2021 Jan. 1;63(9):1525–1529.

[36] Saigal A, Difilippo V, Zimmerman MA. The short and long term properties of a liquid crystalline polymer at elevated temperatures: Characterization and modeling. Journal of Electronic Materials. Springer Science and Business Media LLC; 1997 Jul. 1;26(7):847–851.

[37] Standard Test Method for Evaluation of MR Image Artifacts from Passive Implants: 100 Barr Harbor Drive, Standard 2119-24, ASTM International, West Conshohocken, PA, USA, 2024. [Online]. Available at: https://www.astm.org/f2119-24.html

[38] Young NM, Hoff SR, Ryan M. Impact of Cochlear Implant With Diametric Magnet on Imaging Access, Safety, and Clinical Care. Laryngoscope. 2021 Mar;131(3):E952-E956. doi: 10.1002/lary.28854.

[39] Rupp R, Balk M, Sievert M, Leibl V, Schleder S, Allner M, Iro H, Hoppe U, Hornung J, Gostian AO. Risk of magnetic resonance imaging-induced magnet dislocation for different types of cochlear implants: a single-center retrospective study. J Otolaryngol Head Neck Surg. 2023 Apr 21;52(1):28. doi: 10.1186/s40463-023-00633-w.

[40] Jiles, D. Introduction to Magnetism and Magnetic Materials. 3rd ed. CRC Press. 2015. https://doi.org/10.1201/b18948\

[41] Nordbeck P, Fidler F, Weiss I, Warmuth M, Friedrich MT, Ehses P, Geistert W, Ritter O, Jakob PM, Ladd ME, Quick HH, Bauer WR. Spatial distribution of RF-induced E-fields and implant heating in MRI. Magn Reson Med. 2008 Aug;60(2):312-9. doi: 10.1002/mrm.21475.

[42] Yeung CJ, Susil RC, Atalar E. RF safety of wires in interventional MRI: using a safety index. Magn Reson Med. 2002 Jan;47(1):187-93. doi: 10.1002/mrm.10037.

[43] Dhanasingh, A., DeSaSouza, S. (2022). Evolution of Cochlear Implant Technology over the Last 35 Years. In: DeSaSouza, S. (eds) Cochlear Implants. Springer, Singapore. https://doi.org/10.1007/978-981-19-0452-3_3

[44] Advanced Bionics. HiRes Ultra 3D B2B brochure. 028-M953-02 RevB. Stäfa (Switzerland): Advanced Bionics AG; 2018 [cited 2025 May 15]. Available from: https://cochlearimplanthelp.com/wp-content/uploads/2018/09/advanced-bionics-hires-ultra-3d-b2b-brochure_028-m953-02-revb.pdf